USING IN-SITU AEROSOL OPTICAL PROPERTIES TO DEVELOP A NOVEL AIR QUALITY MONITORING AND DIAGNOSTIC TOOL

A Thesis

by

JOHN MICHAEL ORCUTT

Submitted to the Office of Graduate and Professional Studies of
Texas A&M University
in partial fulfillment of the requirements for the degree of

MASTER OF SCIENCE

Chair of Committee,	Sarah D. Brooks
Committee Members,	Don Collins
	Qi Ying
Head of Department,	Ping Yang

December 2014

Major Subject: Atmospheric Sciences

ABSTRACT

Air quality in urban areas is degraded by locally emitted aerosols and gaseous precursors as well as aerosols that have been transported from other areas. Increased amounts of particulate pollutants are associated with respiratory and cardiac ailments as well as adverse birth outcomes. Aerosols also have an important impact on the Earth's climate via direct and indirect effects. However, there is large uncertainty in how much of an impact aerosols actually have. The work presented here uses the optical properties of urban aerosols to create a new tool which has the potential to be used to differentiate aerosol source, as well as understanding the impact pollution has on the climate.

The Cloud and Aerosol Spectrometer with Polarization (CASPOL) was operated in the field for the first time as a part of NASA's Deriving Information of Surface Conditions from Column and Vertically Resolved Observations Relevant to Air Quality (DISCOVER-AQ). The CASPOL was mounted on top of the 70 meter tall Moody Tower and took continuous samples during the month of September 2013. Aerosol sources can be distinguished using the CASPOL data. When aerosol concentrations are greater than 100 L^{-1}, the CASPOL can distinguish aerosol source with only approximately one hour of data. Thus the CASPOL can be used as an air quality monitoring and diagnostic tool as it can determine aerosol source in near real time.

To better understand the impact pollution has on the Earth's climate, soot was generated in our laboratory and the optical properties were examined. Also, soot was used to generate ice crystals in the Texas A&M University Continuous Flow Diffusion Chamber (CFDC) which was used in conjunction with the CASPOL to measure the optical properties of ice nucleated on soot. The optical properties of

freshly emitted soot were highly variable, but this could be caused to a sampling error which occurred. The CASPOL was able to distinguish between ice that was nucleated heterogeneously on soot and ice that was nucleated heterogeneously on mineral dusts, and homogeneously nucleated ice. Thus the CASPOL can help in the understanding of pollutions direct and indirect impacts on climate.

DEDICATION

Dedicated to my loving wife, Heidi Joy.

ACKNOWLEDGEMENTS

I would first like to thank all of the people who have helped and supported me throughout the process of my Master's degree, especially my advisor, Dr. Sarah Brooks. Throughout my time in graduate school, Dr. Brooks has been there to provide thoughtful insight and help me improve my abilities as a scientist. I am extremely appreciative of everything Dr. Brooks has done throughout my tenure at Texas A&M.

I would also like to thank my committee members Dr. Don Collins, and Dr. Qi Ying for their guidance and insight throughout. Thanks must be given to all the members of my research group, past and present, especially to Kristen Collier, Dr. Andrew Glen, and Dr. Peter Dengh. I also must thank Dr. Barry Lefer and Dr. Lennart Johnsson of the University of Houston for supplying me with ozone concentration and meteorological data from the Moody Tower used in this study. Also, thanks to Dr. Rebecca Sheesly of Baylor University for providing me with the organic carbon and elemental carbon data used. Finally, Dr. Renyi Zhang of Texas A&M University allowed me to borrow his soot generator for an extended amount of time. I must also thank the Texas Air Research Council and the National Science Foundation Environmental Chemistry Division which both provided the funding that allowed this research to occur.

My friends and family have been a huge help to me throughout this process. All of their support is greatly appreciated.

Finally, I would like to thank my amazing wife, Heidi for all of her love, support, encouragement, patience, and help. She was always there for me when I needed it most, and her love and encouragement helped me to keep pushing at even the most

difficult of times. She is the joy of my life. Words can not truly express how grateful I am for everything Heidi has done. Thank you.

TABLE OF CONTENTS

Page

ABSTRACT ii

DEDICATION iv

ACKNOWLEDGEMENTS v

TABLE OF CONTENTS vii

LIST OF FIGURES viii

LIST OF TABLES xii

1. INTRODUCTION 1

2. THE CLOUD AND AEROSOL SPECTROMETER WITH POLARIZATION 7

3. DERIVING INFORMATION ON SURFACE CONDITIONS FROM COLUMN AND VERTICALLY RESOLVED OBSERVATIONS RELEVANT TO AIR QUALITY (DISCOVER-AQ) 10

3.1 Moody Tower 10
3.2 Size and Volume Distributions and Mass Concentrations of Urban Aerosols 14
3.3 Potential Aerosol Sources 23
3.4 Optical Properties of Urban Aerosols 28
3.5 Optical Properties of Fresh and Aged Aerosols 34
3.6 A New Potential Technique in Aerosol Monitoring 39
3.7 Further Analysis of the New Potential Technique in Aerosol Monitoring 43

4. AN ANALYSIS OF HOW SOOT AFFECTS THE CLIMATE DIRECTLY AND INDIRECTLY 49

4.1 Optical Properties of Soot 49
4.2 Optical Properties of Ice Nucleated onto Soot 54

5. CONCLUSIONS 71

REFERENCES 76

LIST OF FIGURES

FIGURE Page

2.1 A schematic of the CASPOL instrument adapted from the DMT DMT Manual (2011). 8

3.1 A schematic of the experimental setup of the CASPOL during DISCOVER-AQ on top of the Moody Tower. 12

3.2 Photograph of the CASPOL setup on top of the Moody Tower. . . . 13

3.3 The number distribution of the total cases in each flow regime. 15

3.4 The volume distribution of the total cases in each flow regime. 16

3.5 The CASPOL estimated daily averaged $PM_{2.5}$ (top) and PM_{10} (bottom) mass concentrations of Houston, Texas for the month of September, 2013 using the density of dust and water as upper and lower bounds. The red bar on the $PM_{2.5}$ plot indicates the EPA's 24 hour average limit. 18

3.6 Locations of the Moody Tower, Clinton, Park Place, and Deer Park TCEQ monitoring sites (map courtesy of Google Earth). 20

3.7 The daily averaged $PM_{2.5}$ mass concentration from the TCEQ Clinton, Park Place, and Deer Park monitoring sites for the month of September, 2013. The red bar at the top of the plot represents the EPA's 24-hour average $PM_{2.5}$ limit. 21

3.8 Meteorological data collected on top of the Moody Tower during the month of September, 2013. 25

3.9 Example of a five day HYSPLIT model back trajectory showing a Ship Channel flow regime from the Ship Channel 0918 case. 26

3.10 A map of the Houston metropolitan area showing the four sources and the direction they came from (Map courtesy of Google Earth). 26

3.11 The five minute average wind direction for the Ship Channel 0918 case (top), an example of a back trajectory from the HYSPLIT model (bottom). 27

3.12 The average backscatter intensity (A) and the depolarization ratio (B) as a function of particle diameter for all cases in each source region. . 29

3.13 The frequency of backscatter intensity for a single CASPOL size bin for the ensemble Ship Channel, Urban, and Ocean cases. Left panel is the 2.5 – 3.0 μm size bin, and the right panel is the 7.2 – 7.9 μm size bin. 31

3.14 The scattering signatures for the combined cases in the Ocean source (A), the Ship Channel source (B), and the Urban source (C). 33

3.15 The average backscatter intensity (A) and the depolarization ratio (B) as a function of particle diameter for fresh aerosols from the 09/24 Ship Channel case, partially aged aerosols from the 09/11 Ship Channel case, and aged aerosols from the 09/13 Ship Channel Case. 37

3.16 The scattering signatures of the fresh aerosol case (A), the aged aerosol case (B), and the partially aged aerosol case (C). 38

3.17 The scattering signatures for the estimate of one hour of data for the Ocean (A), Ship Channel (B), and Urban (C) cases. 41

3.18 The scattering signatures for the estimate of eight hours of data for the total Ocean (A), Ship Channel (B), and Urban (C) cases. 42

3.19 The total backscatter intensity over time, in seconds from midnight, for the Ship Channel 0918 case. The area enclosed in the red bars from 9.0 x 10^4 - 1.0 x 10^5 is the peak in total backscatter intensity that was used in the Ship Channel 0918 short case. 46

3.20 The backscatter intensity (A) and the depolarization ratio (B) as a function of particle diameter for the full Ship Channel 0918 case (red) and the five short peaks found in the backscatter intensity in the 0918 Ship Channel case. 47

3.21 The scattering signatures for the first peak in the backscatter intensity over time plots for the Ship Channel 0918, Ocean 0927, and the Urban 0925 cases. 48

4.1 A schematic of the experimental setup used to generate fresh soot particles and measuring their optical properties using the CASPOL . 49

4.2 The backscatter intensity (A) and depolarization ratio (B) as a function of particle diameter for four different samples of freshly generated soot. 51

4.3 The scattering signatures for the four different samples of freshly emitted soot generated in our laboratory. 53

4.4 A schematic of the Continuous Flow Diffusion Chamber (CFDC) showing the aerosol inlet and the recirculating sheath flow. To evacuate and ice the chamber, a sliding plate is used to connect a water and air pump. A separate CASPOL plate is used to connect the CASPOL to the CFDC for optical property measurements. (Adapted from Glen 2013). 56

4.5 A schematic of the experimental setup of the study of the optical properties of ice nucleated on soot particles using the Texas A&M University CFDC to generate the ice crystals and the CASPOL to measure the optical properties of the crystals. 57

4.6 The average backscatter intensity (A) and the depolarization ratio (B) as a function of particle diameter for two samples of heterogeneous ice crystals nucleated on to soot particles and freshly generated soot. The red bar indicates the size where any particles larger than it are assumed to be entirely ice crystals. 60

4.7 Size distributions of the first and second samples of heterogeneous ice crystals with soot as the nucleus. 61

4.8 The experimental setup for the generation of homogeneous ice (Top), and heterogeneously nucleated ice with mineral dusts as nuclei (Bottom). Adapted from Glen and Brooks (2014). 61

4.9 The average backscatter intensity (A) and the depolarization ratio (B) as a function of particle diameter for heterogeneous ice crystals that were nucleated onto freshly generated soot particles vs heterogeneous ice crystals that were generated onto Arizona Test Dust (ATD), Hematite, White Quartz, and Zeolite mineral dusts. 62

4.10 The average backscatter intensity (A) and the average depolarization ratio (B) as a function of particle diameter for heterogeneously nucleated ice using soot as the IN and homogeneously nucleated ice. . 64

4.11 The backscatter intensity (A) and depolarization ratio (B) as a function of particle size for each initial soot particle diameter and supersaturation ratio with respect to ice. 66

4.12 The scattering signatures for two samples of heterogeneous ice nucleated on freshly generated soot particles, heterogeneous ice nucleated on mineral dusts, and homogeneous ice. 69

4.13 The frequency of backscatter intensity for a single CASPOL size bin for freshly generated soot, the first and second samples of heterogeneous ice nucleated on freshly generated soot particles, heterogeneously nucleated ice on mineral dusts, and homogeneously nucleated ice. Left panel is the 2.5 – 3.0 μm size bin, and the right panel is the 7.2 – 7.9 μm size bin. 70

LIST OF TABLES

TABLE Page

3.1 Rules for using the scattering signatures to differentiate the Ship Channel, Urban, and Ocean aerosol source locations. 32

3.2 The start and end date, the max ozone concentration, the OC/EC ratio and the estimation of the aerosol age for each case of each source. OC and EC data courtesy of Dr. Rebecca Sheesly of Baylor University and O_3 data courtesy of Drs.Berry Leifer and Lennart Johnsson of the University of Houston. 36

3.3 Case, number concentration, and duration of the peaks that were found in the backscatter over time from the Ship Channel 0918, Urban 0925, and Ocean 0927 cases. 45

1. INTRODUCTION

The types of aerosols encountered in an urban area are extremely diverse because urban areas are impacted by biogenic, anthropogenic, local, and transported aerosols. The local aerosols in many urban areas consist of mostly black carbon particles, which are formed in the combustion processes (Bond et al. 2013). Secondary organic aerosols (SOA) are another type of local aerosol found in urban areas. SOA are formed by gas-to-particle partitioning of volatile organic compounds (VOCs) which are released by biogenic and anthropogenic sources (Seinfeld and Pandis 2006). Transported aerosols consist of mineral dusts, sea salt, smoke from biomass burning, pollen, and other biogenic particles (Fulton 1966; Hirst and Hurst 1967; Seinfeld and Pandis 2006; Attwood and Greenslade 2011). Both local and transported aerosols may have a negative impact on human health and the Earths climate.

Human health is impacted adversely by particulate matter. Many studies have shown that long term exposure to high concentrations of particulate matter, especially those particles with diameters less than or equal to 2.5 μm ($PM_{2.5}$) and particles with diameters less than 10 μm (PM_{10}), can cause respiratory and cardiac illnesses, and cause adverse birth outcomes (Schwartz 1993; Brunekreef and Forsberg 2005; Dominici et al. 2006; Sapkota et al. 2010; Savitz et al. 2014; Wu et al. 2014; Rappazzo et al. 2014). Particulate matter is monitored across the United States by the Environmental Protection Agency (EPA). In 2012, the EPA set more stringent National Ambient Air Quality Standards (NAAQS) for particulate matter. For $PM_{2.5}$, the standard is 35 $\mu g/m^3$ for any 24-hour period and for PM_{10} the standard is 150 $\mu g/m^3$ for any 24-hour period. Because particulate matter has a negative impact on health, it is becoming extremely important to consistently monitor particulate matter and to

provide accurate air quality forecasts to officials and the general public so they can take appropriate measures. Further, aerosol source is important because the size, morphology, and composition of an aerosol can vary greatly depending on its source (Steerenberg et al. 2006).

While the aerosol loading in urban environments is dominated by soot particles, transported aerosols also contribute to the total urban aerosol concentrations. A commonly transported aerosol, mineral dust, can have lifetimes of up to a week and can be transported significant distances, especially particles with a diameter of 10 μm or less (Attwood and Greenslade 2011). Mineral dusts that have a diameter larger than 10 μm are more susceptible to removal by deposition processes. Mineral dust causes a net cooling effect of approximately -0.1 Wm^{-2} (IPCC 2013), and it contributes to around 45% of the total aerosol mass loading (Caquineau et al. 2002). The transportation of dust is also vitally important in providing micro-nutrients to the oceans (Duce and Tindale 1991; Uematsu et al. 2003). Natural occurring aerosols can also affect Earths radiative budget indirectly via cloud processes. It has been shown that mineral dusts can act as CCN (Yin et al. 2002; Koehler et al. 2009b) and IN (Chen et al. 1998; DeMott 2003; Kanji and Abbatt 2010; Glen and Brooks 2014). In addition, pollen can act as CCN at low supersaturations (Pope 2010; Griffiths et al. 2012), as well as IN at relatively warm temperatures (Diehl et al. 2001, 2002; von Blohn et al. 2005).

Most air quality forecasts are produced by coupling a meteorological model and a chemical transport model. One example of a model is the Weather Research and Forecasting model with Chemistry (WRF/Chem) with the Model of Aerosol Dynamics, Reaction, Ionization, and Dissolution (MADRID) (known as the WRF/Chem-MADRID) (Zhang 2004; Zhang et al. 2010a,b). The WRF/Chem-MADRID and other air quality forecast models do not always capture particulate matter concen-

trations accurately (Chuang et al. 2011; Zhang et al. 2012, 2013; Yahya et al. 2014) The difference between the forecasted concentrations and actual concentrations can be attributed to uncertainties of emissions of both gaseous precursors and primary particles, meteorological conditions, and chemical reactions (Chuang et al. 2011; Zhang et al. 2013; Yahya et al. 2014). Other methods used in air quality forecasting includes statistical regression models (Huang and Smith 1999; Guldmann and Kim 2001; Bordignon et al. 2002), neural networks (Kolehmainen et al. 2001; Nagendra and Khare 2006), case-based reasoning (Kalapanidas and Avouris 2001), and classification and regression trees (Briggs et al. 2000; Barrero et al. 2006) have all been used. Most of these other means of forecasting have only forecasted gaseous constituents. One exception is neural networks, which have shown promise in their ability to forecast particulate matter (Brunelli et al. 2007; Voukantsis et al. 2011). However, all of these methods of air quality forecasting provide only the concentrations of particulate matter and not the composition or the source of the particles.

Aerosols are very important to the Earths climate. Anthropogenic atmospheric aerosols can affect the Earths radiation budget by as much as -1 Wm^{-2} (IPCC 2013). In a polluted urban environment, a large fraction of the ambient aerosols will be soot particles, which do not have a long lifetime (Bond et al. 2013). Soot particles are highly absorptive and cause a net warming effect in the atmosphere of approximately 0.64 Wm^{-2} (Jacobson 2001; IPCC 2013). Because soot is so highly absorptive, it can effectively reduce the photolysis rate of NO_x. A reduction in the photolysis rate can reduce the formation of ozone by as much as 24 ppbv (Dickerson et al. 1997). However, this relationship between soot and ozone can be complicated by the composition of the soot particle as well as any coatings the soot particle has accrued (Hansen et al. 2000; Jacobson 2001, 2006). Ozone can undergo chemical reactions that create the products that condense onto the soot particle. For example, recent

laboratory measurements found that the ozone and α-pinene reaction occurs much faster than once thought (Ma et al. 2013). This reaction forms products which coat soot particles on the order of hours. Coated soot particles have different optical properties then un-coated soot particles (Bond et al. 2006; Khalizov et al. 2009, 2013; Adachi and Buseck 2013; Lan et al. 2013; Wang 2013). Some coated soot particles are not as highly absorbing as they were when they originated (Adachi and Buseck 2013; Lan et al. 2013; Wang 2013). Because these coated soot particles are not as absorptive, they no longer have much of an impact on photolysis rates and remove less ozone. However, soot particles coated in non-absorbing material will actually be more absorbing than fresh soot (Bond et al. 2006), and thus will decrease the photolysis rate of NO_x even more. Aged soot particles can also affect the Earths radiative budget indirectly. Un-coated soot is hydrophobic, but studies have shown that the aging process makes soot more hydrophilic and that these aged and coated soot particles can act as cloud condensation nuclei (CCN) (Kotzick and Niessner 1999; Lary et al. 1999; Decesari et al. 2002; Zuberi et al. 2005; Koehler et al. 2009a; Khalizov et al. 2009, 2013) and ice nuclei (IN) (DeMott et al. 1999; Gorbunov et al. 2001; Koehler et al. 2009a). The optical, physical, and chemical properties of aged soot particles are areas that need to be researched further.

Because of aerosols ability to affect the climate, it is vital to understand how they scatter light. Light scattered by spherical particles in the atmosphere can be calculated by Lorenz-Mie theory, but Lorenz-Mie theory is only valid for spherical particles (Bohren and Huffman 2008; Morgan et al. 2010). All of the aforementioned aerosols: soot, mineral dust, pollen, and other biological aerosol are non-spherical particles. Particle size, composition, age, shape, morphology, refractive index, number concentration, and size distributions all effect aerosol optical properties. This greatly increases the complexity of modeling the scattering properties of non-spherical

particles. There are multiple approaches to modeling the scattering properties of non-spherical properties. The T-Matrix (Mishchenko et al. 1997), Discrete Dipole Approximation (DDA), and Improved Geometric Optics Methods (IGOM) are methods that can be used to model the optical properties for particles with specified geometries (Bi et al. 2009). These methods make broad approximations, but are more precise then Lorenz-Mie theory which can only be used to represent spherical particles.

There have been many studies that investigate the in-situ optical properties of non-spherical particles; however, these properties are usually determined for an ensemble of particles (Arakawa et al. 1998; West et al. 1997; Curtis et al. 2008; Attwood and Greenslade 2011). Glen and Brooks (2013) measured the single particle optical properties of thirteen different dusts over a scattering angle of 4° to 12° in the forward direction and 168° to 176° in the backwards direction using the Cloud and Aerosol Spectrometer with Polarization (CASPOL). This instrument was also able to measure the perpendicular polarization in the backwards direction. With this instrument, Glen and Brooks were able to calculate a depolarization ratio, which can be used to differentiate spherical particles from non-spheres (Sassen 1991; Mishchenko et al. 1997). They found that the backscatter and polarized backscatter intensities varied with particle size for all thirteen dust types, and using a new optical signature method, they were able to classify twelve of the thirteen dusts into three distinct groups.

The Cloud Aerosol Spectrometer with Depolarization (CASPOL) is a newly developed aerosol optical properties instrument developed and manufactured by Droplet Measurement Technologies and is being tested in our laboratory at Texas A&M University (Glen and Brooks 2013, 2014). The CASPOL could potentially be used to determine aerosol source and composition as well as aid in short-term air quality forecasting. It can also be used to help quantify the direct and indirect

impacts aerosols have on the Earth's climate. In this study, the potential for the CASPOL to be implemented as an air quality monitoring and diagnostic tool by differentiating between various atmospheric particle types and sources will be fully tested.

2. THE CLOUD AND AEROSOL SPECTROMETER WITH POLARIZATION

The Cloud and Aerosol Spectrometer with Polarization (CASPOL) is a new optical particle counter (OPC) developed by Droplet Measurement Technologies (DMT) and tested in our laboratory at Texas A&M University (Glen and Brooks 2013, 2014). This instrument has the forward scattering and backward scattering detection capabilities of DMT's Cloud and Aerosol Spectrometer (CAS) sensor of the Cloud Aerosol and Precipitation Spectrometer (CAPS) (Baumgardner et al. 2001, 2011), but has two additional capabilities that the CAPS instrument does not. The first additional capability is that the CASPOL has an additional detector in the backwards direction that can measure the perpendicularly polarized backscatter intensity. Secondly, the CASPOL measures optical properties on a particle-by-particle basis.

In order to measure the light scattered by aerosols, the CASPOL uses a linearly polarized laser at a wavelength of 680 nm. As seen in Figure 1, there are a total of four detectors in the instrument; two in the front, and two in the back. In the forwards direction there is a qualifying detector and a forward scatter detector. The qualifying detector allows any particle that passes within 0.75 mm of the center of the laser beam to be measured for a large size range of particles from 0.6 to 50 μm. The forward scatter detector calculates the diameter of each particle using Mie theory. In the backwards direction there is a detector that measures the backscatter intensity and another detector that measures the perpendicularly polarized backscatter intensity. The forward detectors have collection angles of 4° to 12°, and the backward detectors have collection angles of 168° to 178°. It is important to note that the diameter that the CASPOL measures is the water equivalent diameter and not the geometric diameter. Thus, in this manuscript the term diameter will be used to refer to the

water equivalent diameter.

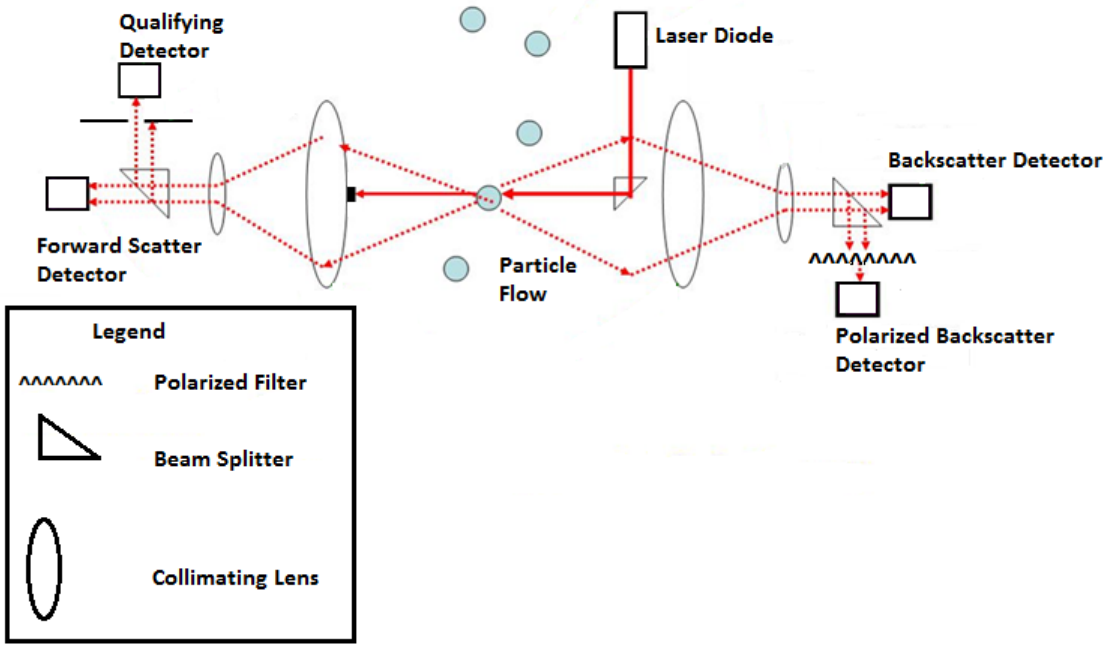

Figure 2.1: A schematic of the CASPOL instrument adapted from the DMT DMT Manual (2011).

The CASPOL is unique among optical particle counters because of the perpendicularly polarized backscatter detector and because it can measure optical properties on a particle-by-particle basis. A depolarization ratio (δ) can be defined using the perpendicularly polarized backscatter ($\beta_{\perp}$) and the perpendicularly polarized backscatter ($\beta_{\parallel}$) (Equation 1). The depolarization ratio can be used to differentiate between spherical and non-spherical particles. A spherical particle will have a depolarization ratio of zero and a non-spherical particle will have a depolarization ratio greater than zero (Sassen 1991; Mishchenko et al. 1997). For example, the depolarization ratio

has been used to distinguish ice crystals from water droplets (Nicolet et al. 2010; Glen and Brooks 2014). Because of the additive nature of the optical properties, the particle-by-particle data an be used to calculate the optical properties of an ensemble. Using the CASPOL, concentration, size distribution, backscatter intensity, and depolarization ratio can be determined.

$$\delta = \frac{\beta_{\perp}}{\beta_{\parallel}} \tag{2.1}$$

3. DERIVING INFORMATION ON SURFACE CONDITIONS FROM COLUMN AND VERTICALLY RESOLVED OBSERVATIONS RELEVANT TO AIR QUALITY (DISCOVER-AQ)

In the fall of 2013, the Cloud and Aerosol Spectrometer with Polarization (CASPOL) was operated as a part of NASA's *D*eriving *I*nformation on *S*urface conditions from *CO*lumn and *VER*tically resolved observations relevant to *A*ir *Q*uality (DISCOVER-AQ) in Houston, Texas. DISCOVER-AQ is a five year field campaign that is organized by NASA. So far, the field campaign has occurred in the Baltimore-Washington Corridor, the Houston, Texas metropolitan area, and Colorado. The mission of the DISCOVER-AQ field campaign is to use in-situ measurements of gaseous constituents and particulate matter as well as aircraft and ground based lidars to improve the remote sensing abilities of air pollution. The following section discusses the data collected by the CASPOL and the development of a new air quality monitoring and forecasting tool. By using the particle-by-particle optical property data that the CASPOL measures, a scattering signature can be produced. With this scattering signature, aerosol sources and types can be determined, and these scattering signatures could potentially be used as an air quality monitoring and forecasting tool for near real time identification of aerosol source and type.

3.1 Moody Tower

The Houston segment of DISCOVER-AQ was the first field deployment of the CASPOL since being designed and built by DMT. From August 28 through October 4, 2013, the CASPOL was located on top of the Moody Tower. The Moody Tower is located at 29.7176° N, -95.3414° W, which is approximately four kilometers south of downtown Houston, Texas. The inlet was located on top of the building which is

approximately 70 meters tall. The height of the tower is low enough that the aerosols being sampled are representative of the aerosols at the surface, but tall enough so that any intermittent point sources will not interfere with the measurements. The inlet was specially designed to rotate so that it always points into the wind. The inlet was connected to a 1.5 meter long heated pipe, to better control the conditions of the flow, (Quinn et al. 1998) by a $\frac{3}{4}$ inch outer diameter piece of non-conductive tubing that was 2.5 meters long. A dump line with a flow rate of 10 L Min^{-1} was teed off at the end of the inlet line. The CASPOL was connected to the tee with the dump line, and behind the CASPOL was a thermocouple, relative humidity meter, HEPA filter, another thermocouple and then another relative humidity meter as seen in Figure 3.1. A photograph of the CASPOL setup on top of the Moody Tower is shown in Figure 3.2. Other measurements taken concurrently at the Moody Tower include O_3, CO, NO, NO_x, NO_y, SO_2 concentrations, and basic meteorological parameters collected by Dr. Barry Lefer and Dr. Lennart Johnsson of the University of Houston, and a seven channel aethelometer and $PM_{2.5}$ and TSP filter samplers were operated by Dr. Rebecca Sheesly of Baylor University.

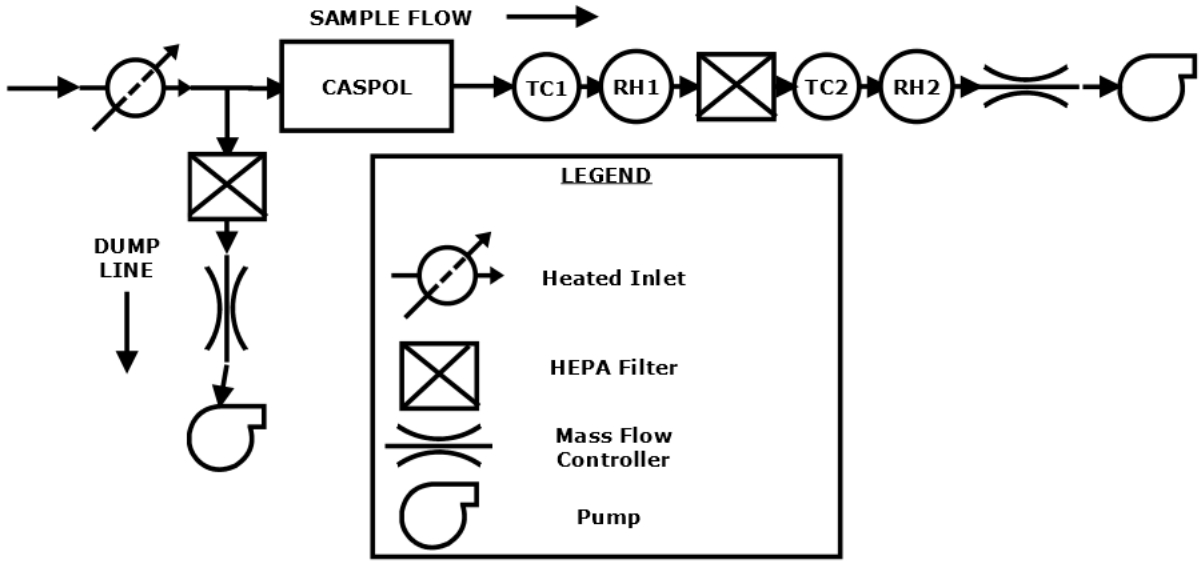

Figure 3.1: A schematic of the experimental setup of the CASPOL during DISCOVER-AQ on top of the Moody Tower.

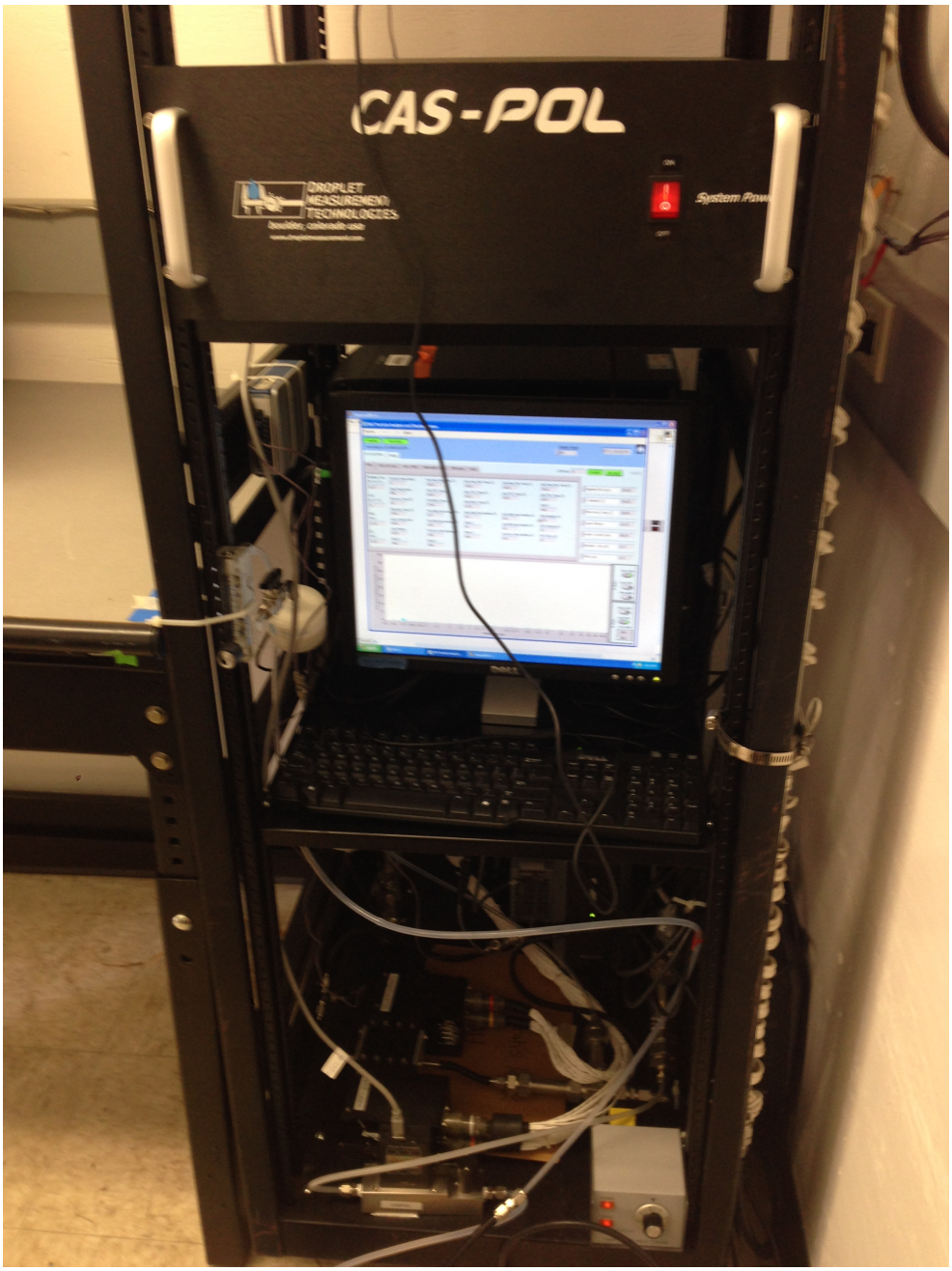

Figure 3.2: Photograph of the CASPOL setup on top of the Moody Tower.

3.2 Size and Volume Distributions and Mass Concentrations of Urban Aerosols

Using the CASPOL, we were able to calculate number and volume distributions and were able to estimate the mass concentrations of the Houston aerosols. As seen in Figure 3.3, the total number distribution of each flow regime is shown. The distributions are about what would be expected, with the peak of the distribution in the sub-micron size range and the slope decreasing towards larger sizes. All three flow regimes have similar number distributions and cannot be distinguished from each other off only the number distribution. Volume distribution of the three flow regimes is seen in Figure 3.4. The volume distributions have the usual primary peak at sub-micron sizes as expected, and the beginnings of a secondary peak at larger sizes (5 μm and up) was also captured. There are some unexpected peaks such as the peak in the Ship Channel at approximately 1 μm. However, there is still not much different between the cases to distinguish them using only their volume distributions either. Thus the optical properties must be observed in order to potentially differentiate the cases.

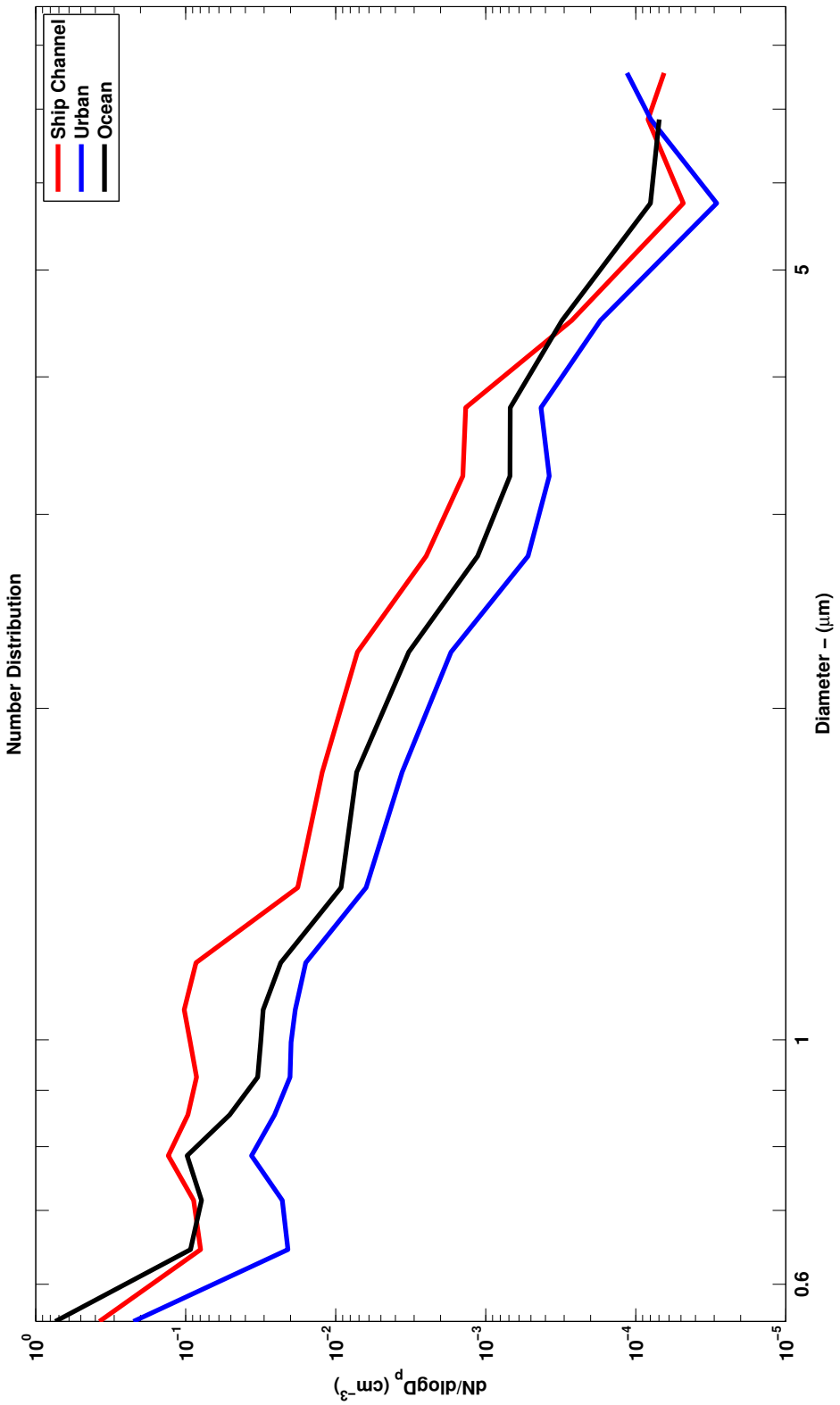

Figure 3.3: The number distribution of the total cases in each flow regime.

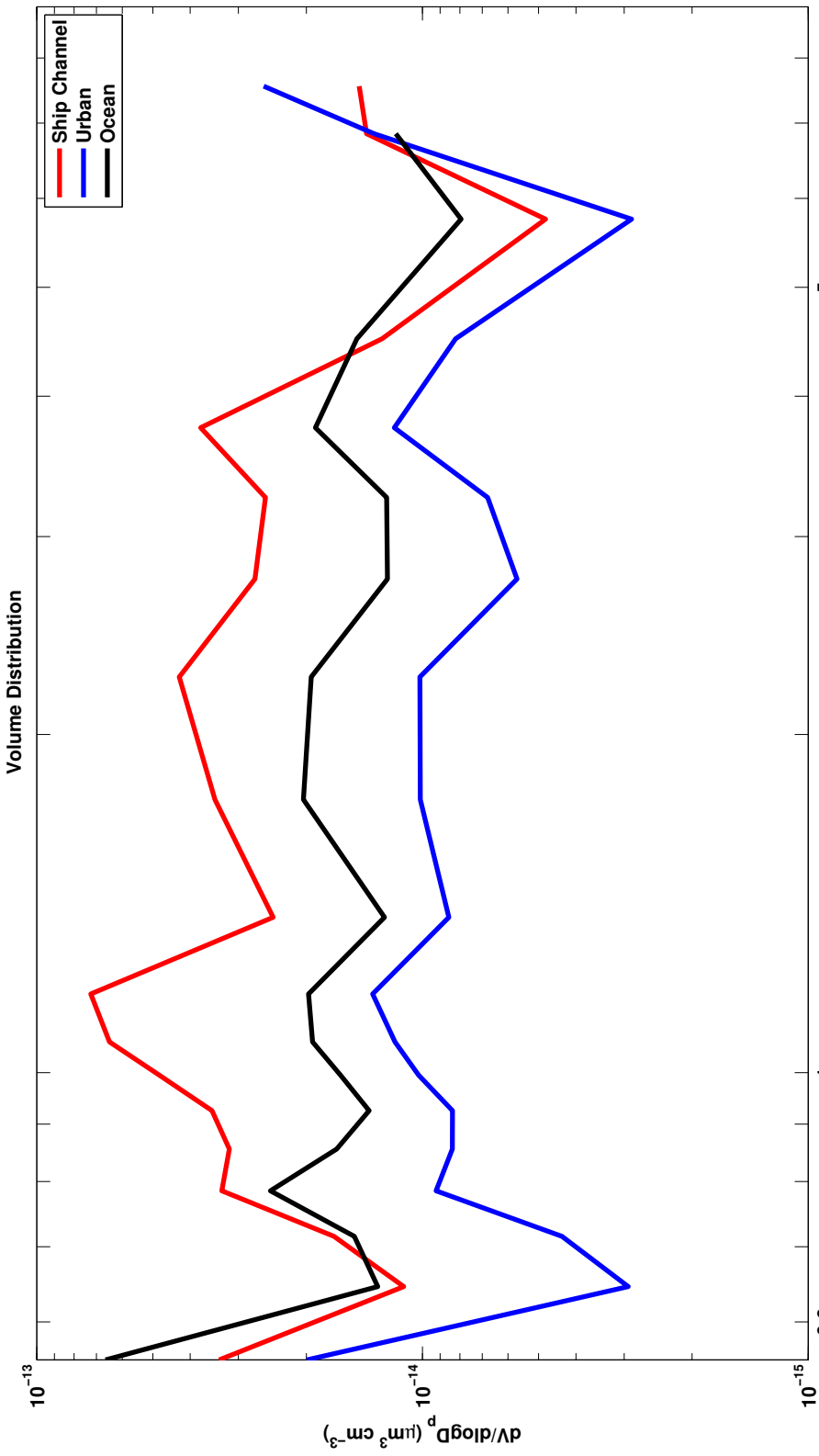

Figure 3.4: The volume distribution of the total cases in each flow regime.

Particulate matter is monitored throughout the United States by the EPA in terms of a mass concentration in micro-grams per cubic meter (μg m^{-3}). Using the CASPOL, a mass concentration of aerosols can be estimated. It is important to note that the mass concentrations derived from the CASPOL data are only an estimate of the mass concentrations as the CASPOL only measures optical water equivalent diameter and not the aerodynamic diameter. Also the CASPOL does not measure the mass of the particle, and thus a particle density must be assumed. To calculate $PM_{2.5}$ we summed up the CASPOL size bins from 0.5 to 2.5 μm, and for PM_{10} we summed up the size bins from 0.5 to 10.2 μm because the CASPOL does not have a 10 μm size bin. Then we created volume distributions for both $PM_{2.5}$ and PM_{10}. To convert volume to mass, we used the density of dust, 1.71 g cm^{-3}, and of water, 1.0 g cm^{-3} to represent the upper and lower boundaries of the density (Smettem 2006; Hiranuma et al. 2011). Daily averaged $PM_{2.5}$ mass concentration for the month of September 2013 is seen in the top panel of Figure 3.5, and in the bottom panel of Figure 3.5 the daily averaged PM_{10} mass concentration for the month of September 2013 is shown. The red bar at 35 μg/m^{-3} is the EPA maximum 24 hour average limit of $PM_{2.5}$. It is only violated three times according to the CASPOL's estimations. The PM_{10} daily limit is not plotted because the mass concentrations are never near the limit of 150 μg/m^{-3}. There is only a slight difference between the $PM_{2.5}$ and PM_{10} mass concentrations which implies that the majority of the particles sampled are 2.5 μm and smaller.

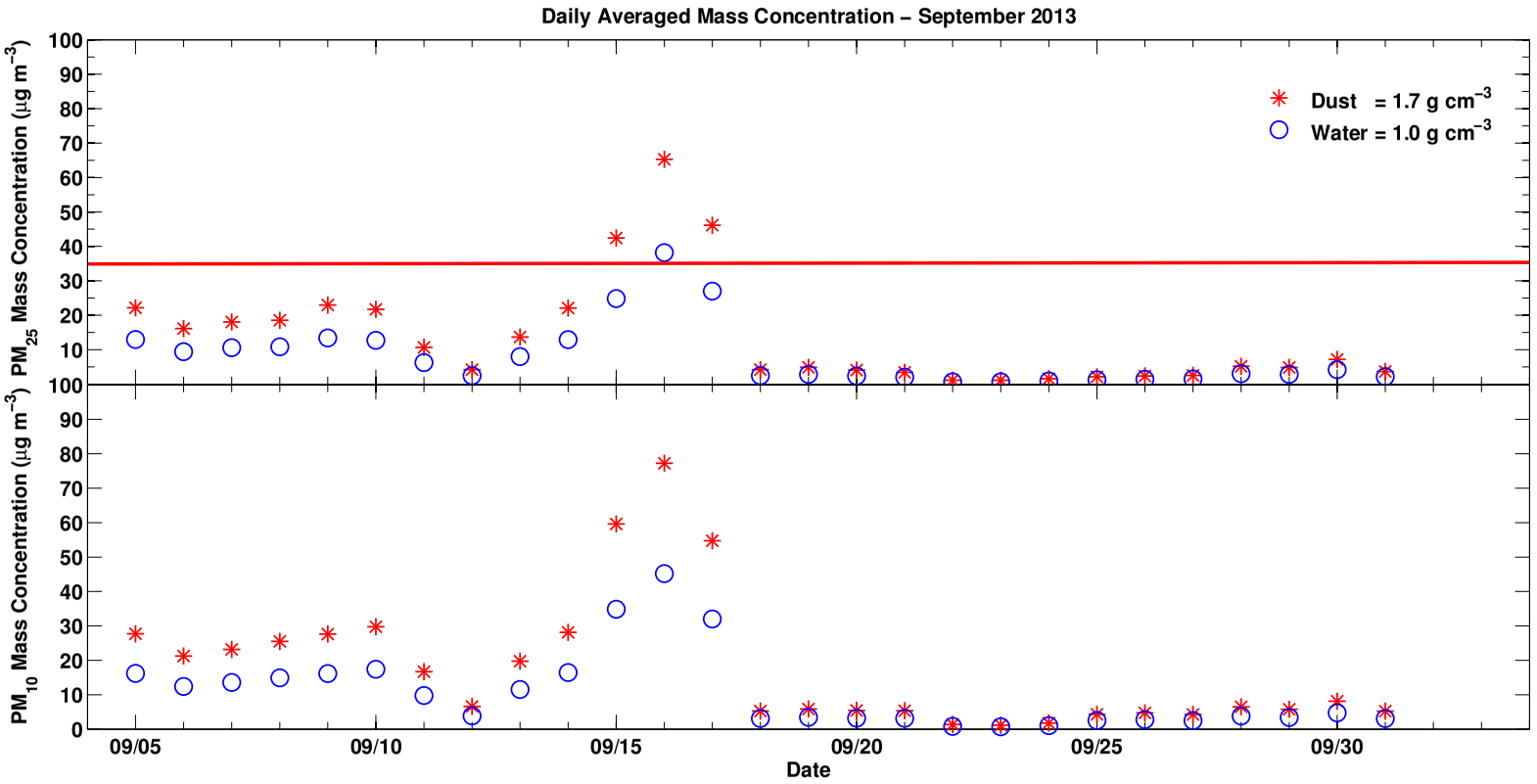

Figure 3.5: The CASPOL estimated daily averaged $PM_{2.5}$ (top) and PM_{10} (bottom) mass concentrations of Houston, Texas for the month of September, 2013 using the density of dust and water as upper and lower bounds. The red bar on the $PM_{2.5}$ plot indicates the EPA's 24 hour average limit.

The Texas Commission for Environmental Quality (TCEQ) monitors particulate matter at many of their monitoring sites. The TCEQ has numerous air quality monitoring stations across the state of Texas. The Park Place TCEQ monitoring site is the closest to the Moody Tower at approximately 5 km to the south east, and the Deer Park TCEQ monitoring site is the furthest from Moody Tower at approximately 20 km. The Clinton TCEQ monitoring site is in between the other two at around 8 km. The locations of these monitoring sites are shown in Figure 3.6. As seen in Figure 3.5, there is a steep and sudden drop off in both $PM_{2.5}$ and PM_{10} concentrations around September 17, 2013. This sudden drop off can also be seen the the TCEQ particulate matter data collected at the Clinton, Park Place, and Deer Park monitoring sites (Figure 3.7). As seen in Figure 3.7, the mass concentration begins to decrease on 09/16 then there is a primary peak ten days later on 09/26. While in the CASPOL's derived particulate matter plots (Figure 3.5), the mass concentration starts to decrease on 09/17, and the second peak is completely missed. The CASPOL's estimation of mass concentration exceeds the $PM_{2.5}$ daily limit three times, while the mass concentrations from the TCEQ monitoring sites never exceed the EPA's limits. It is important to remember that the CASPOL can only estimate mass concentration as it does not measure the mass of the particle, and it measures the water equivalent diameter and not the aerodynamic diameter. However, this only explains why the CASPOL's estimated mass concentrations are much higher than the actual mass concentrations, and not as to why the CASPOL missed the second peak.

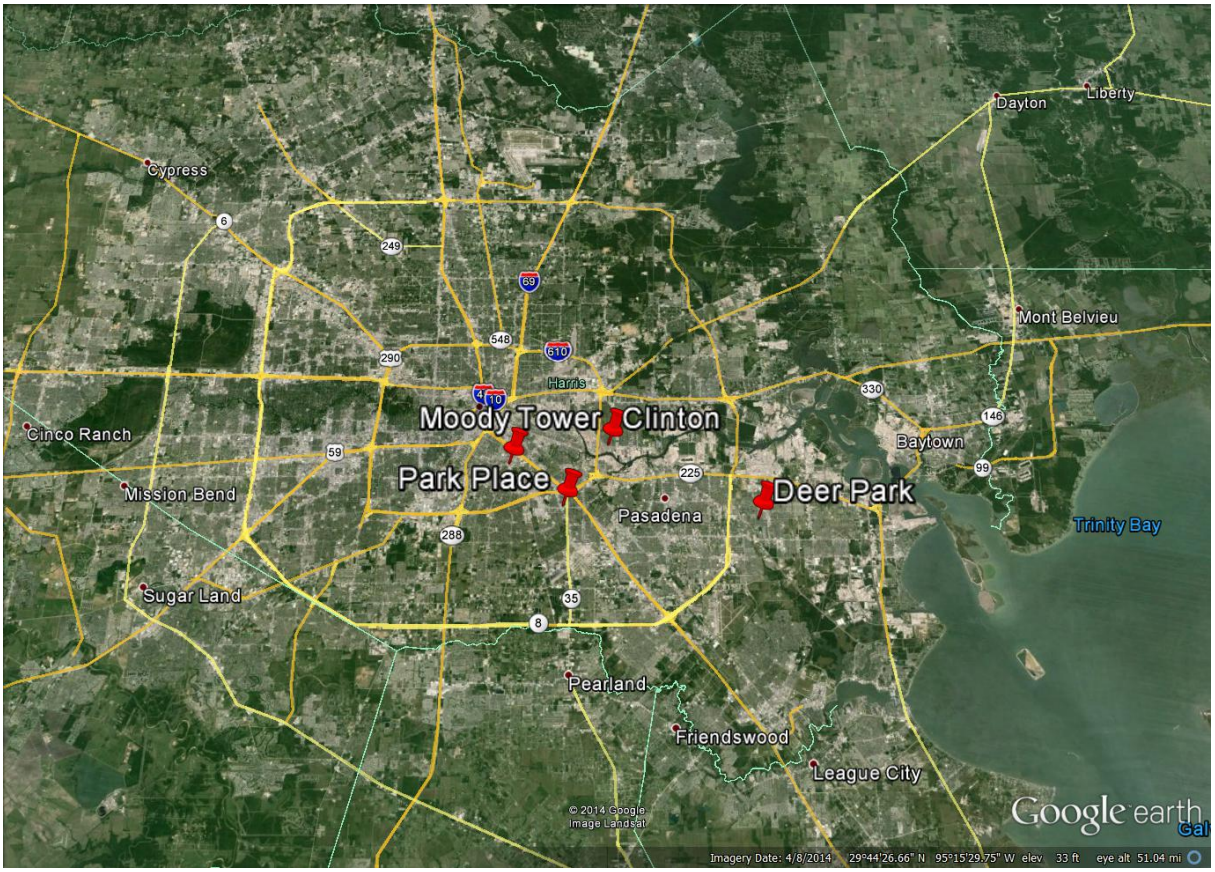

Figure 3.6: Locations of the Moody Tower, Clinton, Park Place, and Deer Park TCEQ monitoring sites (map courtesy of Google Earth).

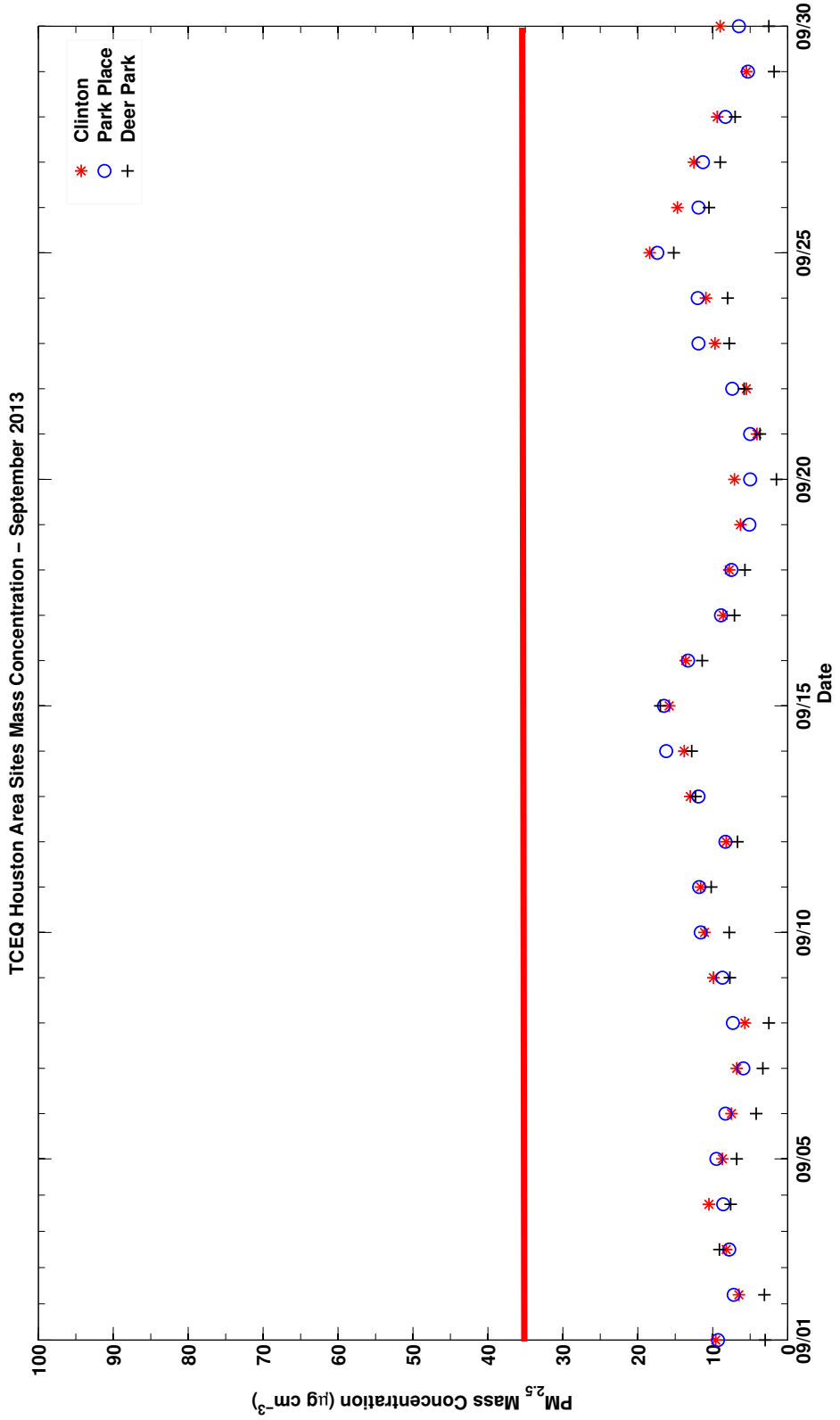

Figure 3.7: The daily averaged $PM_{2.5}$ mass concentration from the TCEQ Clinton, Park Place, and Deer Park monitoring sites for the month of September, 2013. The red bar at the top of the plot represents the EPA's 24-hour average $PM_{2.5}$ limit.

To provide possible insight on the sudden drop off in mass concentration we turn to meteorological data collected on top of the Moody Tower by the University of Houston. Figure 3.8 shows the raw five minute average temperature, pressure, wind speed, wind direction, precipitation, and relative humidity for the month of September, 2013. As seen from the rainfall graph in Figure 3.8, a storm occurred in area late in the day on 09/16. Approximately one inch of rain fell in a relatively short period of time. This storm coincides nicely with the start of the decrease in mass concentration in the TCEQ data and in the CASPOL estimated mass concentration. Thus this decrease in both the TCEQ mass concentration and CASPOL mass concentration can be explained by the wet deposition process removing the majority of the particles. However, after this storm, the CASPOL mass concentration never recovers. Rather, it stays very low for the remainder of the month while the TCEQ mass concentrations recover around ten days later. A frontal passage occurs on 09/21, and there is a noticeable dip in the TCEQ mass concentrations on 09/21. This frontal passage can be seen in the meteorological data plotted in Figure 3.8, as the temperature and pressure sharply decrease, and there is rain fall in the same time period. After this frontal passage, the winds remained out of the east, north, and the north east for approximately one week. At the beginning of the project, the winds were from the south. Through the middle of the project, the winds were mostly from the south east. The winds had not blown from the northerly directions for as long of a time period, and could be a factor in why the CASPOL's mass concentrations never recovered. However, the winds returned to a more south easterly flow during the last four days of the project. Other possible factors are that the Clinton, Park Place, and Deer Park TCEQ monitoring sites are all only ten meters above ground level, and are located in close proximity to busy road ways or industrialized areas, while the CASPOL is mounted nearly 70 meters above ground level, 1 km from any major highway

and in a more residential area. There is also the possibility that moisture entered the inlet line either by condensation or precipitation that was drawn into the inlet. Mass concentrations can be estimated by the CASPOL, but it must be used only as an estimator and not for any regulatory purposes, as location and meteorological conditions can have a large impact on the measurements.

3.3 Potential Aerosol Sources

Air masses over the Moody Tower are likely to experience four major aerosol sources. The Ship Channel source, which is a heavily industrialized area on the east side of Houston. The Urban source, which consists of the urban center of Houston. The Ocean source, which consist of transported aerosols from the Gulf of Mexico. Lastly the Rural source, which consists of transported aerosols from the west. Conveniently, these sources come from four different wind directions relative to the Moody Tower. Aerosol flow regimes were determined using the NOAA, Atmospheric Resources Laboratories Hybrid Single Particle Lagrangian Integrated Trajectory (HYSPLIT) model (Draxler and Hess 1997, 1998; Draxler et al. 1999) to create five day back trajectories with six hour intervals using Global Data Assimilation (GDAS) model data with 0.5 degree resolution (Figure 3.9). The regimes were determined by the angle at which the wind was coming into the measurement site using the HYSPLIT back trajectories. If the back trajectories show the wind coming from 45° to 135° the source is the ship channel; 135° - 225° the ocean; 225° - 315° rural; 315° to 45° urban (Figure 3.10). If rainfall amounts exceeded half an inch in the six hours before or during the case, the case was discarded due to the likelihood of the majority of particles being removed via the wet deposition process. In total, five ship channel cases, three urban cases, and two ocean cases were eligible to be used for further analysis of the scattering properties.

Models often poorly characterize the winds in the boundary layer in urban areas due to the increased surface roughness. To check the validity of the cases determined by the HYSPLIT back trajectories, the five minute average wind direction, which measured on top of the Moody Tower, was compared to the HYSPLIT output. Figure 3.9 illustrates the HYSPLIT output for the Ship Channel 0918 case, and Figure 3.11 shows the five minute average wind direction for the Ship Channel 0918 case. The HYSPLIT shows that the surface winds (red line and triangles) are from the south east at approximately 135 ° at the Moody Tower. The five minute averaged wind direction for the entire case is not always less than 135 ° cutoff angle for the Ship Channel case. However, for the majority of the time, the direction is never more than ten degrees away from the cutoff, and the average for the time period is 125 °, well below the maximum angle allowed. Thus, the use of the HYSPLIT back trajectories for determining the aerosol flow cases is valid. The remainder of the cases are similar to the previous one where the five minute average wind direction is usually within ten degrees of the angle the HYSPLIT back trajectory shows.

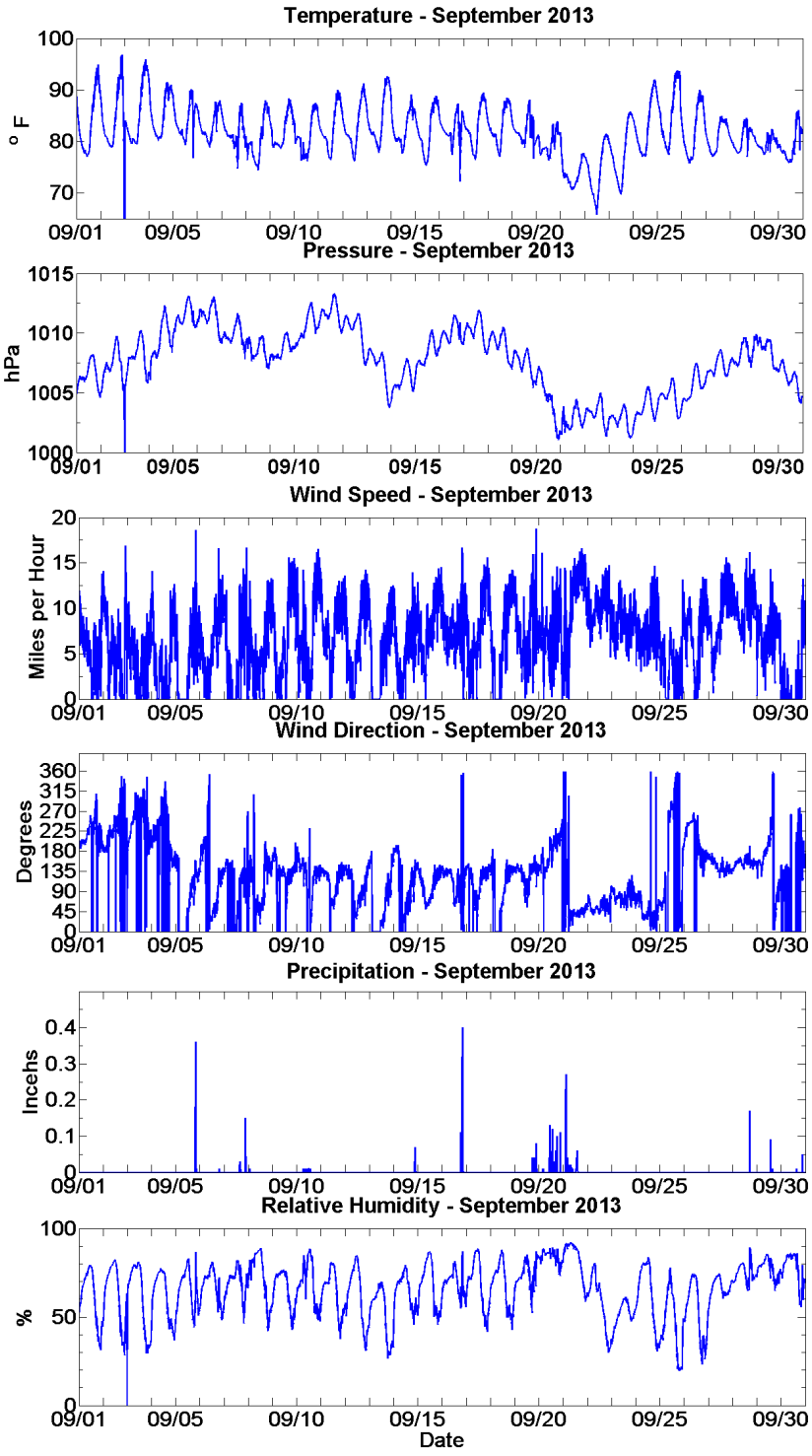

Figure 3.8: Meteorological data collected on top of the Moody Tower during the month of September, 2013.

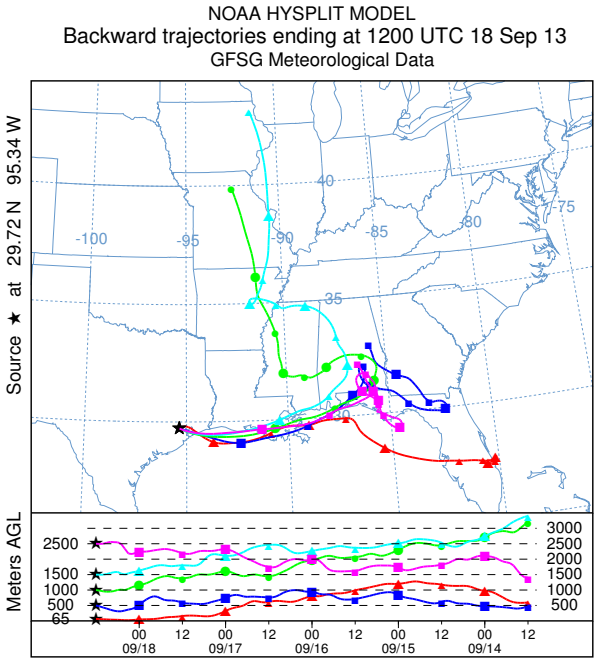

Figure 3.9: Example of a five day HYSPLIT model back trajectory showing a Ship Channel flow regime from the Ship Channel 0918 case.

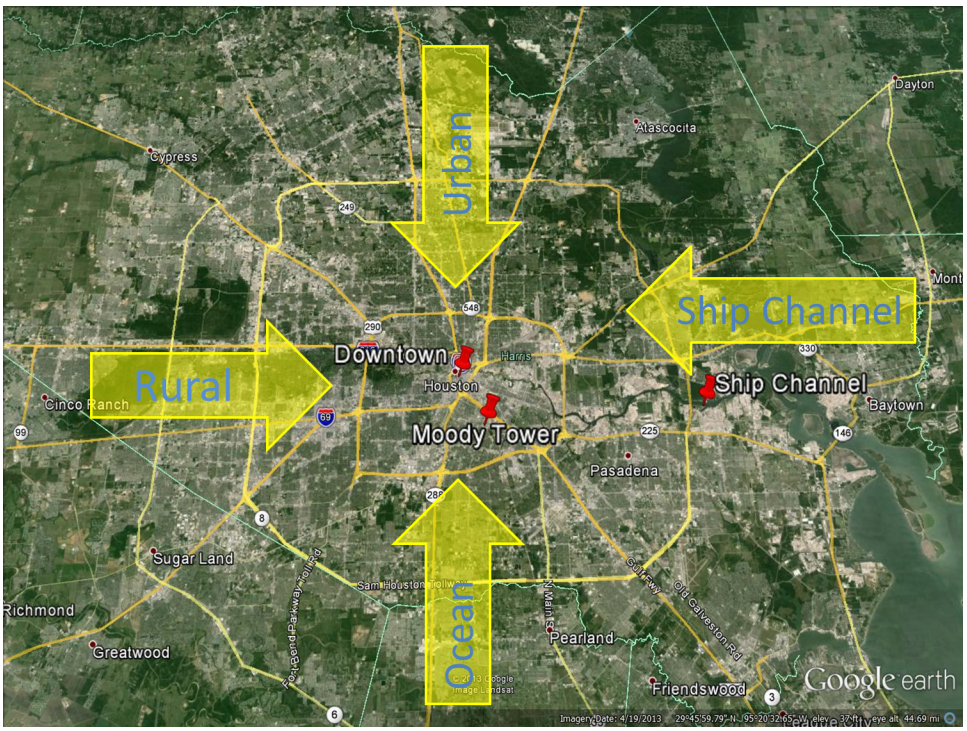

Figure 3.10: A map of the Houston metropolitan area showing the four sources and the direction they came from (Map courtesy of Google Earth).

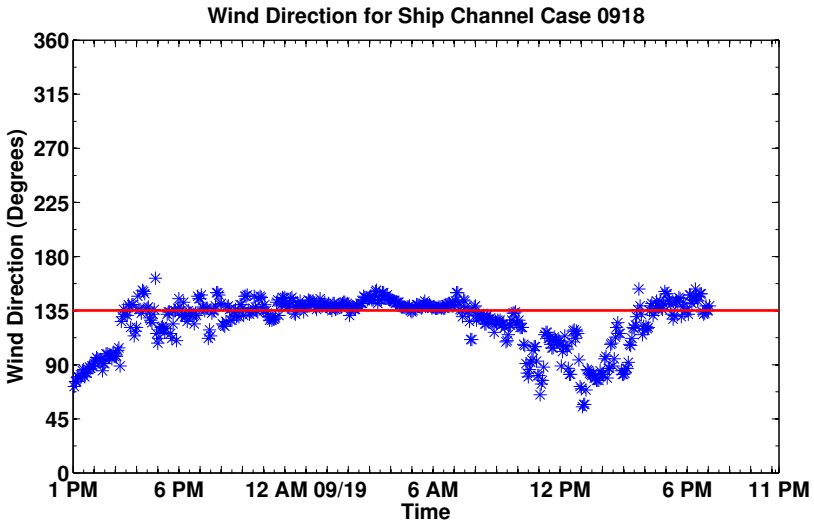

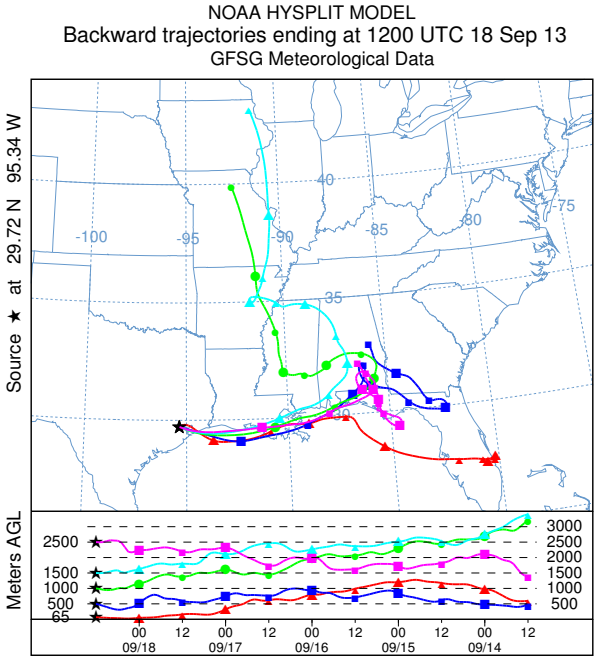

Figure 3.11: The five minute average wind direction for the Ship Channel 0918 case (top), an example of a back trajectory from the HYSPLIT model (bottom).

3.4 Optical Properties of Urban Aerosols

The average backscatter intensity and the depolarization ratio as a function of particle diameter have been shown for the average of ensemble of cases for each source region (Figure 3.12). The bars represent one slandered deviation above and below the mean. The backscatter intensity gives an insight into the size and shape of a particle, and the depolarization ratio gives insight into whether a particle is spherical or non-spherical. A particle with a depolarization ratio of zero is spherical, and a particle with a depolarization ratio greater zero is non-spherical. As can be seen in Figure 3.12A, the backscatter intensity generally increases as size increases for all three cases. It is very similar for all three cases in the smaller sizes below 2 μm. At 2 μm, the Urban case has a slightly higher backscatter intensity. However, the standard deviations overlap at all particles diameter. Figure 3.12B shows that the Ocean case is more depolarizing than the other two cases followed by the Ship Channel which is more depolarizing than the Urban case. The depolarization ratio for all cases approaches zero between 0.7 and 1 μm. This indicates that in that size range a large portion of the particles were spherical. These spherical particles could potentially be hygroscopic particles that have taken up water because of the high relative humidities routinely experienced in Houston. For the sizes above 1 μm, the particles are clearly non-spherical for all cases. Both the Ship Channel and Urban cases contain much larger particles than the Ocean case. There is no real distinction between the cases only using Figure 3.12; however, using a new scattering signature technique developed by Glen and Brooks (2013) is used in an effort to distinguish the cases from each other.

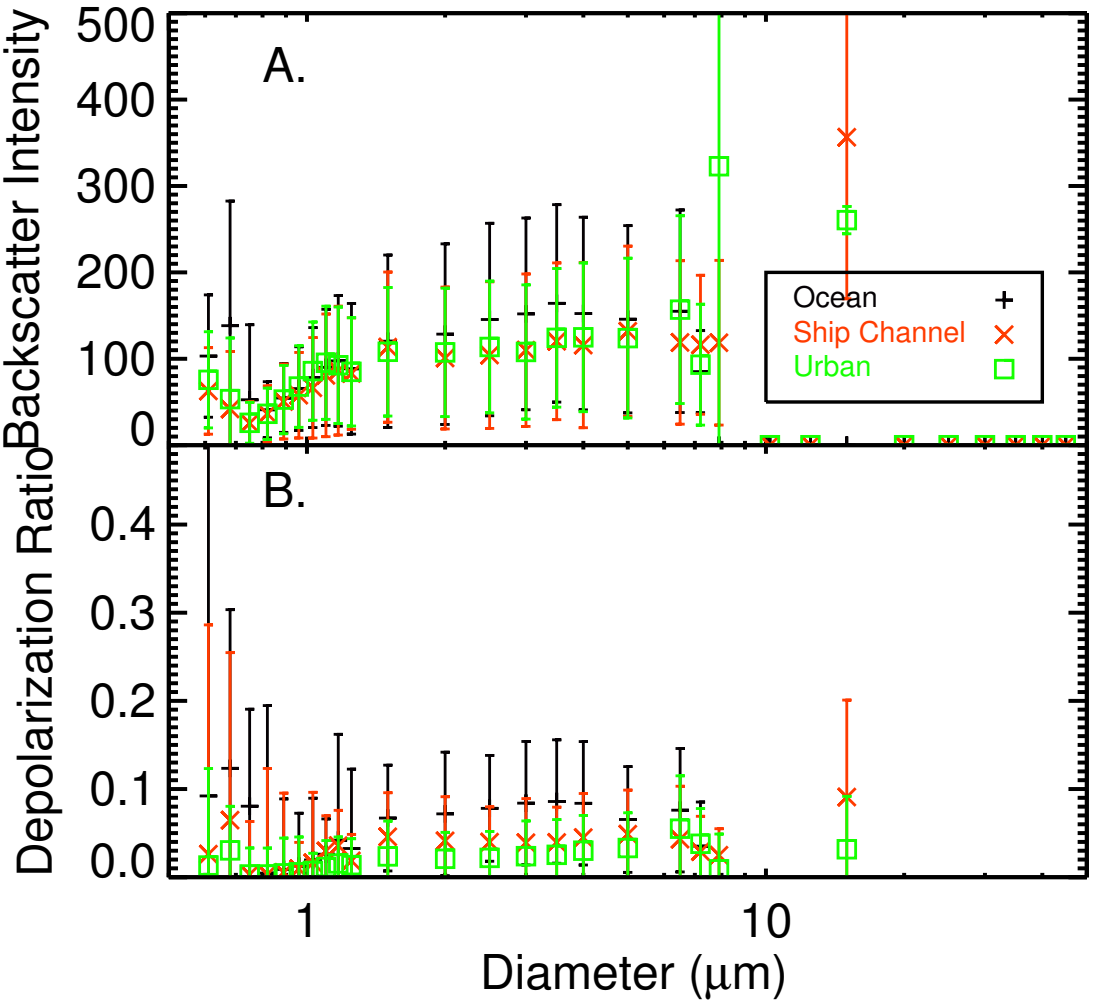

Figure 3.12: The average backscatter intensity (A) and the depolarization ratio (B) as a function of particle diameter for all cases in each source region.

The frequency of particles at a give backscatter intensity for the 2.5 – 3.0 μm and the 7.2 – 7.9 μm size bins for the entire Ship Channel, Urban, and Ocean flow regimes is shown in Figure 3.13. The colors represent a percentage of particles at a particular backscatter intensity. As seen, the distribution of backscatter intensity for all three regimes for both size bins is quite variable, ranging from 0 – 1200 a.u. The Ocean case has the largest variance in both size bins, while the Urban case has the least variance. The majority of the particles sampled have a backscatter intensity located between 50 – 200 a.u. for the 2.5 – 3.0 μm size bin and between 0 – 250 for the 7.2 – 7.9 μm size bin. The large variance of backscatter intensity at a single size bin indicates that there are many different particle shapes being sampled. Using this backscatter distribution at a single size bin helps to illustrate the many different particle shapes that were sampled.

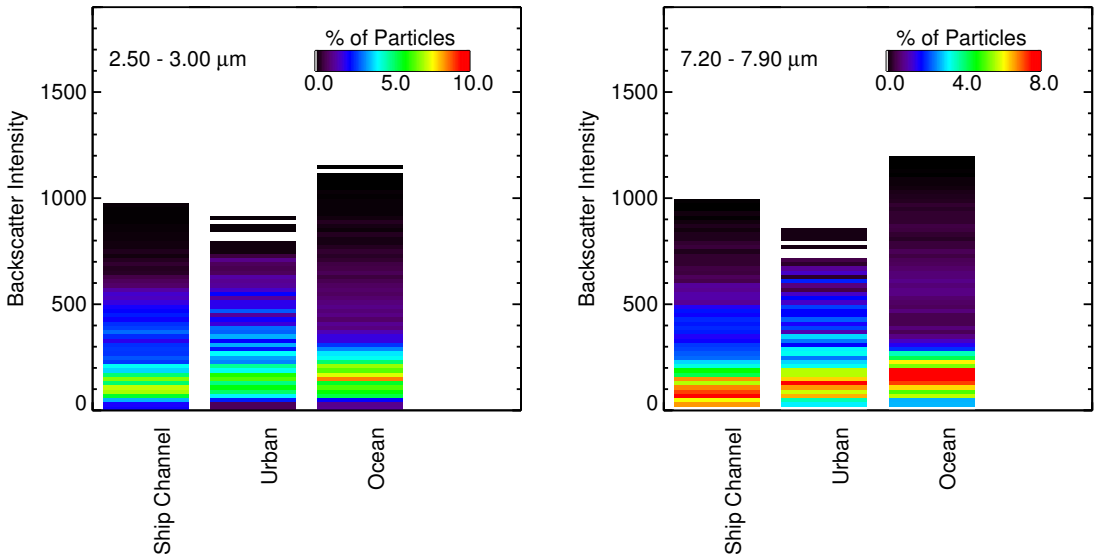

Figure 3.13: The frequency of backscatter intensity for a single CASPOL size bin for the ensemble Ship Channel, Urban, and Ocean cases. Left panel is the 2.5 – 3.0 μm size bin, and the right panel is the 7.2 – 7.9 μm size bin.

The new scattering signature technique was originally developed by Glen and Brooks (2013). To create the scattering signatures, the backscatter intensity and depolarization ratio are first discretized. Next, the frequency of particles that have intersecting values are placed in each bin. The color of each bin indicates the percentage of particles that have intersecting values. In Figure 3.14, the composite scattering signatures of each flow regime is shown. The Ocean cases, seen in Figure 3.14A, have the strongest backscatter intensity, approaching 400, and is the most depolarizing. The Ship Channel cases (Figure 3.14B) is slightly depolarizing but the backscatter intensity is around half of the Ocean cases at around 210. The Urban cases has an even lower backscattering intensity of 200 and is the least depolarizing at approximately 0.1 (Figure 3.14C). Rules for classifying aerosols by source area

using the scattering signature technique are shown in Table 3.1. By using this scattering signature technique, the CASPOL can distinguish aerosol source regions in the Houston area. The CASPOL's ability to distinguish aerosol source shows that a potential exists for the CASPOL to be a useful tool in air quality monitoring and forecasting. However, it should be noted that these signatures of each regime are a composite of several cases which span multiple hours. For the CASPOL to be effective as an air quality monitoring and diagnostic tool, it must be able to distinguish aerosol sources using scattering signatures created with a short time frame of data.

Backscatter Intensity vs. Depolarization Ratio			
	Ship Channel	**Urban**	**Ocean**
Shape	**Steep Curve**	**Semi-Circle**	**Shallow Curve**
Depolarization Ratio	**<0.7**	**<0.1**	**<1.0**
Backscatter Intensity (a.u.)	**<250**	**<200**	**<400**
Maximum % of Particles	**0.05**	**0.01**	**0.10**

Table 3.1: Rules for using the scattering signatures to differentiate the Ship Channel, Urban, and Ocean aerosol source locations.

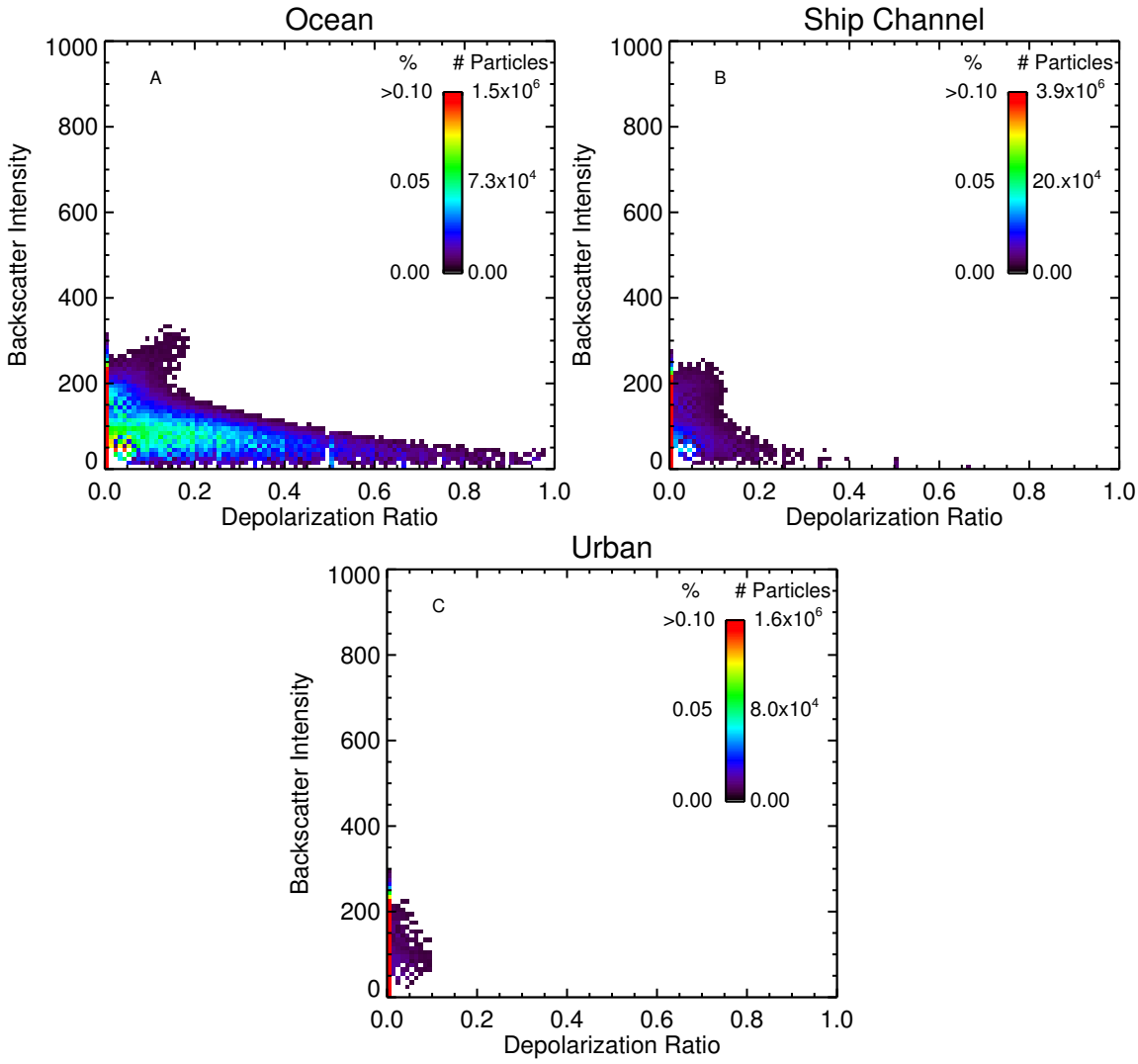

Figure 3.14: The scattering signatures for the combined cases in the Ocean source (A), the Ship Channel source (B), and the Urban source (C).

3.5 Optical Properties of Fresh and Aged Aerosols

It is known that ozone can interact with soot particles and change the hygroscopicity of the soot particle (Ma et al. 2013). This can cause the soot particle to take up water at ambient relative humidities which changes the soot particles optical properties. Volatile organic compounds (VOCs) are released by both biogenic and anthropogenic processes and are a precursor to secondary organic aerosols (SOA). VOCs can also condense onto $PM_{2.5}$ and PM_{10} changing the optical properties of the particles. Using aethelometer data from Dr. Rebecca Sheesly of Baylor University, an elemental carbon to organic carbon ratio (OC/EC) can be determined. Elemental carbon (EC) is freshly emitted black carbon, and organic carbon (OC) is any other carbonaceous particle including aged black carbon. The OC/EC ratio gives us information as to whether the aerosols are fresh and directly emitted, if particles have undergone some form of coating, or if they were formed via gas-to-particle partitioning. Using OC/EC ratios and O_3 concentration, from the University of Houston, we have determined if aerosols are fresh or aged in each case and examined the optical properties. Because soot is such a major component of the total aerosol load in urban areas, it is important to better understand the optical properties of both aged and fresh soot particles.

Table 3.2 shows the individual cases, the start date and time, end date and time, O_3 concentration, OC/EC ratio, and an estimation of whether the aerosols are fresh, aged, or some intermediate value. An estimation of the aerosols age was determined using the O_3 concentration and OC/EC ratios. O_3 concentrations were classified into three ranges: high, ranging from 0 – 33 ppbv; medium, ranging from 33 – 66 ppbv; and low, ranging from 66 – 100 ppbv. OC/EC ratios were classified into two groups, high (above 10), and low (below 10). Pöschl et al. (2001) found that under

standard atmospheric conditions soot will age with an O_3 concentration of 30 ppbv, and Schurath and Naumann (1998) found that O_3 concentrations of 100 ppbv can oxidize soot. A normal OC/EC ratio for an urban area is around 6 (Seinfeld and Pandis 2006). Generally if the O_3 concentration was low and the OC/EC ratio was low (below 10), than the aerosols were assumed to be fresh. If the O_3 concentration was high and the OC/EC ratio was high as well (above 10), than the aerosols were assumed to be aged. For any other OC/EC ratio and O_3 concentrations, the age was assumed to be partially aged.

A comparison of the average backscatter intensity and the depolarization ratio as a function of particle diameter between a fresh aerosol case (Ship Channel 0923), partially aged aerosol case (Ship Channel 0911), and an aged aerosol case (Ship Channel 0914) is shown in Figure 3.15. As seen, the fresh case backscatters more light and has a higher depolarization ratio than the partially aged and aged cases. Interestingly, the partially aged case is has a lower backscatter intensity and is less depolarizing than both the fresh and aged cases. The scattering signatures of the fresh and aged aerosols are not very different from each other (Figure 3.16). The aged case is has a slightly higher backscattering intensity and is more depolarizing than the fresh case, and the aged case is somewhat bimodal compared to the fresh case. The partially aged case has a similar backscatter intensity as the other two, but is much more depolarizing than the fresh and aged cases. The optical properties of estimated fresh, partially aged, and aged cases of aerosols seem to be very similar. However, the scattering signature of partially aged aerosol case is much more depolarizing than the other two cases. More research should be done to further our knowledge of the optical properties of aged aerosols.

Case	Start Date	Start Time	End Date	End Time	Max [O_3] (ppbv)	[O_3] Level	OC/EC	Estimation of Age
Urban	09/21	1 AM	09/22	7 AM	30.6	Low	21.3	Partially Aged
Urban	09/22	1 PM	09/22	7 PM	42.0	Moderate	21.7	Aged
Urban	09/25	1 PM	09/25	7 PM	91.9	High	12.6	Aged
Ocean	09/27	4 AM	09/27	11 AM	53.1	Moderate	10.3	Partially Aged
Ocean	09/28	1 PM	09/29	1 PM	39.2	Moderate	8.6	Partially Aged
Ship Channel	09/11	2:30 PM	09/12	6 AM	54.6	Moderate	6.6	Partially Aged
Ship Channel	09/13	7 PM	09/14	7 PM	74.4	High	10.7	Aged
Ship Channel	09/18	1 PM	09/19	7 PM	46.4	Moderate	2.9	Fresh
Ship Channel	09/24	12 AM	09/24	6 AM	22.1	Low	9.4	Fresh
Ship Channel	09/27	12 PM	09/28	6 AM	60.1	Moderate	9.5	Partially Aged

Table 3.2: The start and end date, the max ozone concentration, the OC/EC ratio and the estimation of the aerosol age for each case of each source. OC and EC data courtesy of Dr. Rebecca Sheesly of Baylor University and O_3 data courtesy of Drs.Berry Leifer and Lennart Johnsson of the University of Houston.

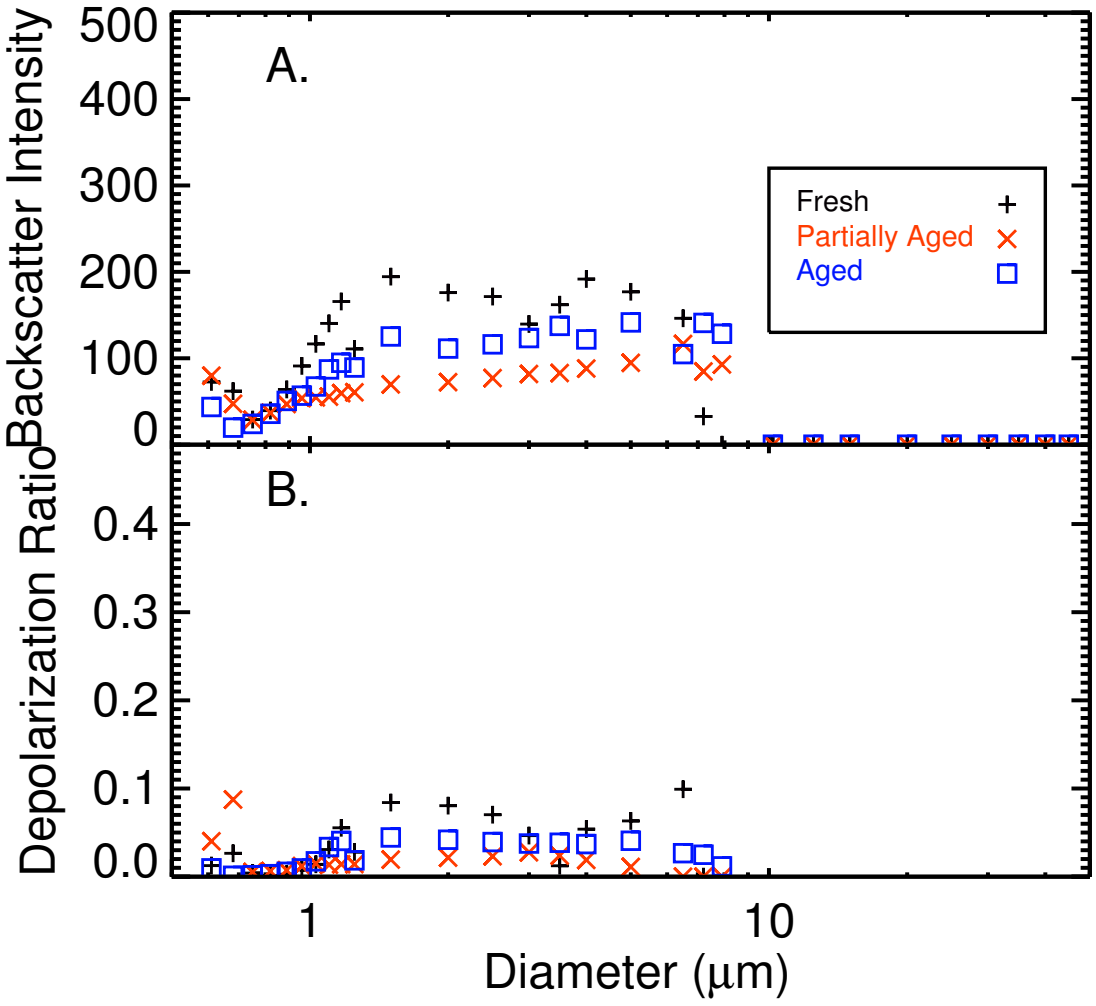

Figure 3.15: The average backscatter intensity (A) and the depolarization ratio (B) as a function of particle diameter for fresh aerosols from the 09/24 Ship Channel case, partially aged aerosols from the 09/11 Ship Channel case, and aged aerosols from the 09/13 Ship Channel Case.

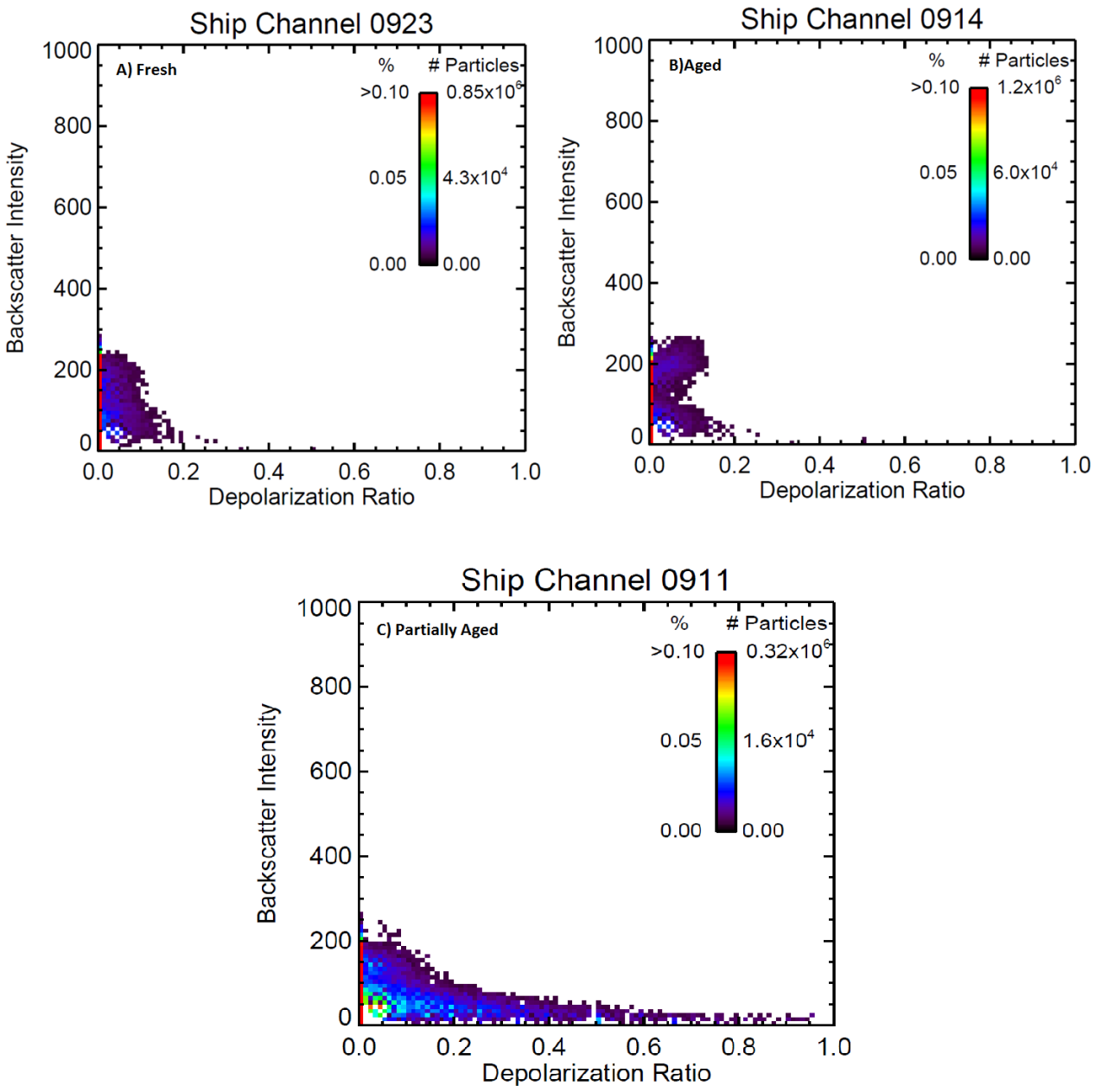

Figure 3.16: The scattering signatures of the fresh aerosol case (A), the aged aerosol case (B), and the partially aged aerosol case (C).

3.6 A New Potential Technique in Aerosol Monitoring

To determine the feasibility of using the CASPOL as an air quality monitor and a short-term air quality monitoring and diagnostic tool, scattering signatures were made using one and eight hours of data for each case. The average number concentration of all the cases was calculated to determine the number of particles that the CASPOL might sample in one and eight hours. Using the average number concentration of 94.8 L^{-1} and the standard CASPOL flow rate of 1.2 L Min^{-1}, the number of particles that the CASPOL might sample in one hour is approximately 7,000, and the number of particles that might be sampled in eight hours is approximately 55,000. Scattering signatures were then created for each case using only 7,000 particles for one hour of data and 55,000 particles for eight hours of data. The scattering signatures for one hour of data are shown in Figure 3.17. With a number concentration of 94.8 L^{-1}, one hour of data is not enough to recreate scattering signatures that are representative of the original cases. With eight hours of data, the recreated scattering signatures are distinguishable from the originals. There are some differences between the scattering signatures using the full data sets (Figure 3.14) and the scattering signatures created using eight hours of data (Figure 3.18). The scattering signatures created using eight hours of data from each case (Figure 3.18) closely follow the scattering signature rules defined in Table 3.1 in section 3.4 of this manuscript. Even though the estimated one hour of data is not enough data for the CASPOL to recreate scattering signatures of aerosol source regions, the CASPOL can still be used as an air quality monitor and as a short term air quality forecasting tool because the estimated eight hours of data is enough to reliably determine aerosol source regions. Eight hours is a useful amount of time for air quality monitoring because the US EPA uses eight hour average limits for many critical pollutants. It is also important to note that the number concentration

used in these calculations seems low because it is the average of all the cases, which span many hours and conditions. With a higher number concentration, the CASPOL would need less time to recreate the aerosol source scattering signature accurately.

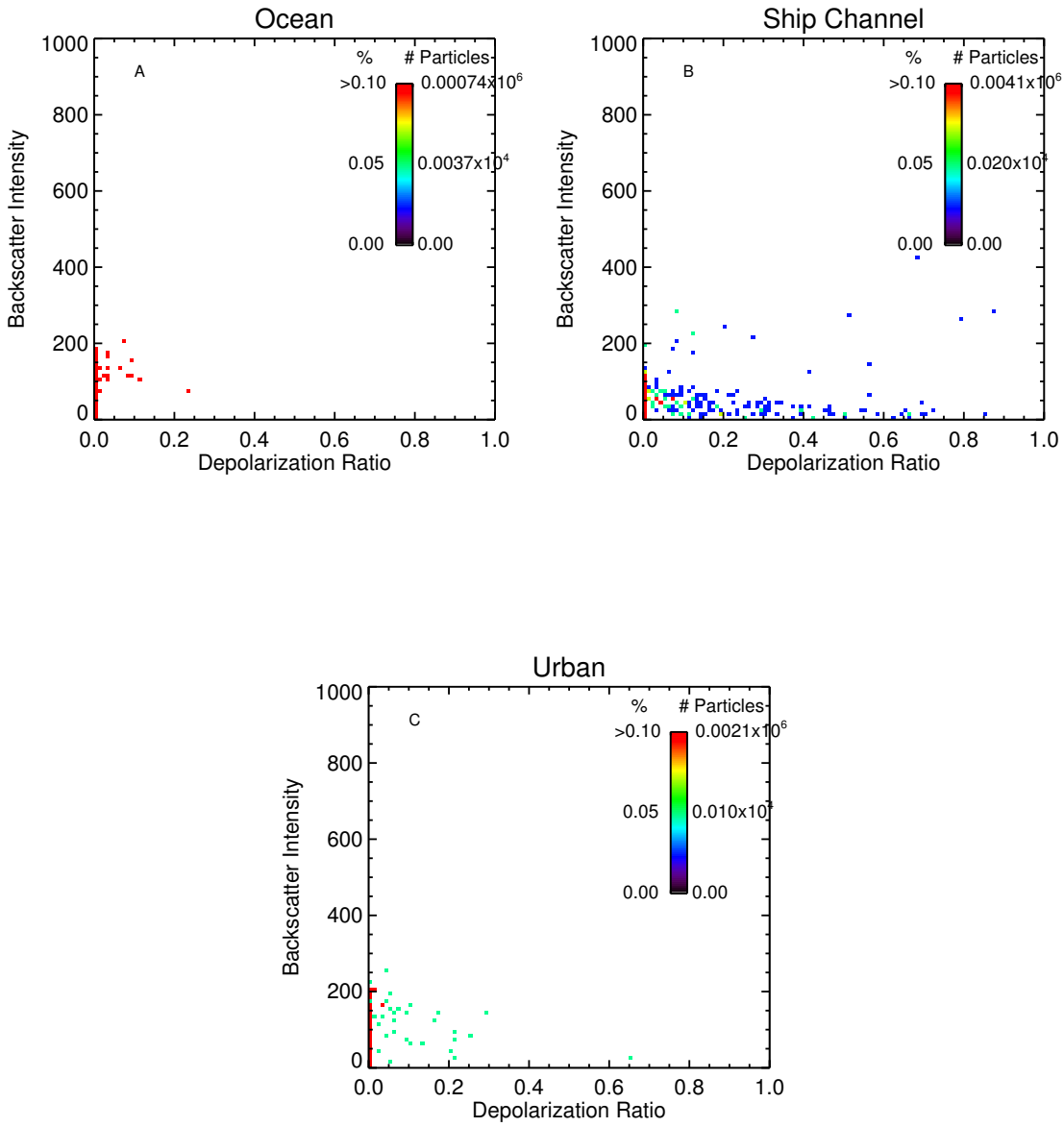

Figure 3.17: The scattering signatures for the estimate of one hour of data for the Ocean (A), Ship Channel (B), and Urban (C) cases.

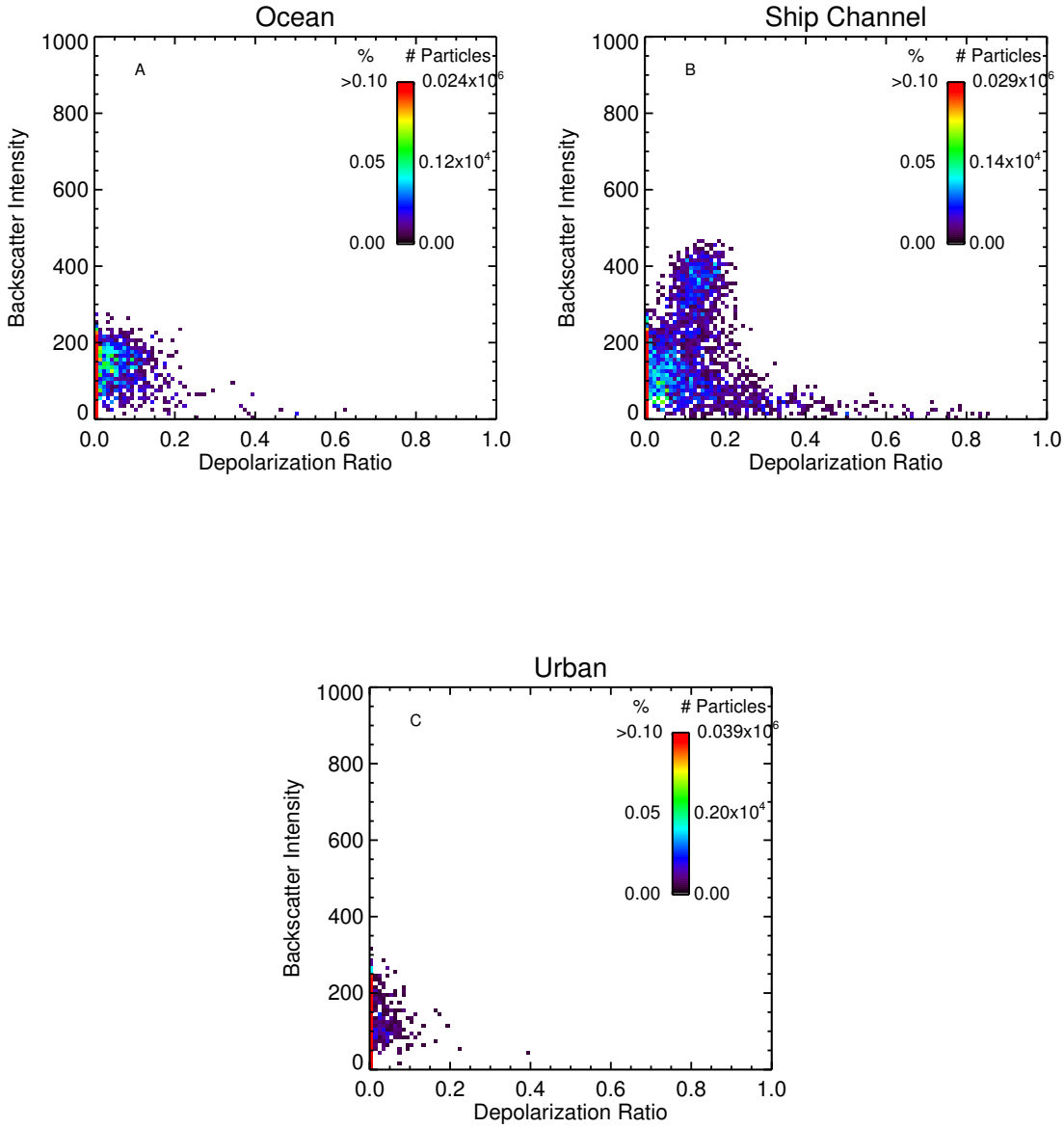

Figure 3.18: The scattering signatures for the estimate of eight hours of data for the total Ocean (A), Ship Channel (B), and Urban (C) cases.

3.7 Further Analysis of the New Potential Technique in Aerosol Monitoring

To continue examining the CASPOL's ability to be used as a short-term air quality monitoring and forecasting tool, the backscatter intensity over time was plotted for a case in the Ship Channel, Ocean, and Urban flow regimes. Then the time series of the total backscatter intensity was examined for any unusual or large peaks. Table 3.3 contains the number of peaks found in each of the three cases, the number concentration during the peak, and duration of the peak. The backscatter intensity plotted over time for the Ship Channel 0918, Urban 0925, and the Ocean 0927 cases are shown in Figure 3.19. Identified peaks are numbered and enclosed between the bars. Next the optical properties for the abbreviated time periods were examined. The average backscatter intensity and the depolarization ratio as a function of particle diameter of the Ship Channel 0918 peaks (black symbols) are plotted against the full Ship Channel 0918 case (red cross) in Figure 3.20. Both the backscatter intensity and depolarization ratio are similar for both the peaks and the full Ship Channel 0918 case with the peaks being slightly more depolarizing and they have a slightly larger backscatter intensity in sizes above 1.5 μm. The backscatter intensity and the average depolarization ratio as a function of particle diameter are similar for the other short term cases as well. Scattering signatures were created for each peak identified. The scattering signatures for the first peak in the Ship Channel 0918, Ocean 0927, and the Urban 0925 cases are shown in Figure 3.21. Interestingly, all of the scattering signatures for the peaks are similar to the scattering signature for each aerosol source. Using the rules for determining the aerosol source as defined in section 3.4, Table 3.1 in this manuscript, the Ship Channel Peak 1 case follow all the rules. However, the Urban Peak 1 case is more depolarizing than the rules allow, but the case is in agreement with the other three rules, and the Ocean 0927 Peak 1 case

is not as depolarizing as the rules state. Thus the majority of each cases scattering data originates from a small amount of time.

An interesting thing to note is that these peaks all span a relatively short amount of time. For example the first peak in the Ship Channel 0918 case is only approximately 2.75 hours in duration. However, this peak has a scattering signature that is representative of the Ship Channel scattering signature. This is due to the fact that the number concentration during this peak was 275.6 L^{-1}. Earlier in this section, scattering signatures were created using the average number concentration of all the cases of 98.4 L^{-1}, to simulate one hour of data. This number concentration proved to be insufficient to recreate the scattering signatures with one hour of data. It has just been shown, however, that if the number concentration is high enough (around 200 L^{-1} +), than the CASPOL can create a scattering signature that is representative of the aerosol source with only a few hours of data. These results implicate that under certain conditions the CASOPL can be an extremely useful air quality monitoring and diagnostic tool used to identify aerosol source in near real time. This rapid determination of aerosol source can lead to better responses by the public during times of poor air quality due to particulate matter.

Case	Peak Number	Number Concentration (L^{-1})	Duration (Hours)
Ship Channel 0918	1	275.6	2.75
	2	265.6	1.5
	3	99.5	2.5
	4	143.1	2.5
	5	498.6	3
Urban 0925	1	85.4	0.75
	2	36.6	0.75
	3	17.4	0.25
Ocean 0927	1	43.3	1.5
	2	348.9	1.25
	3	267.0	1

Table 3.3: Case, number concentration, and duration of the peaks that were found in the backscatter over time from the Ship Channel 0918, Urban 0925, and Ocean 0927 cases.

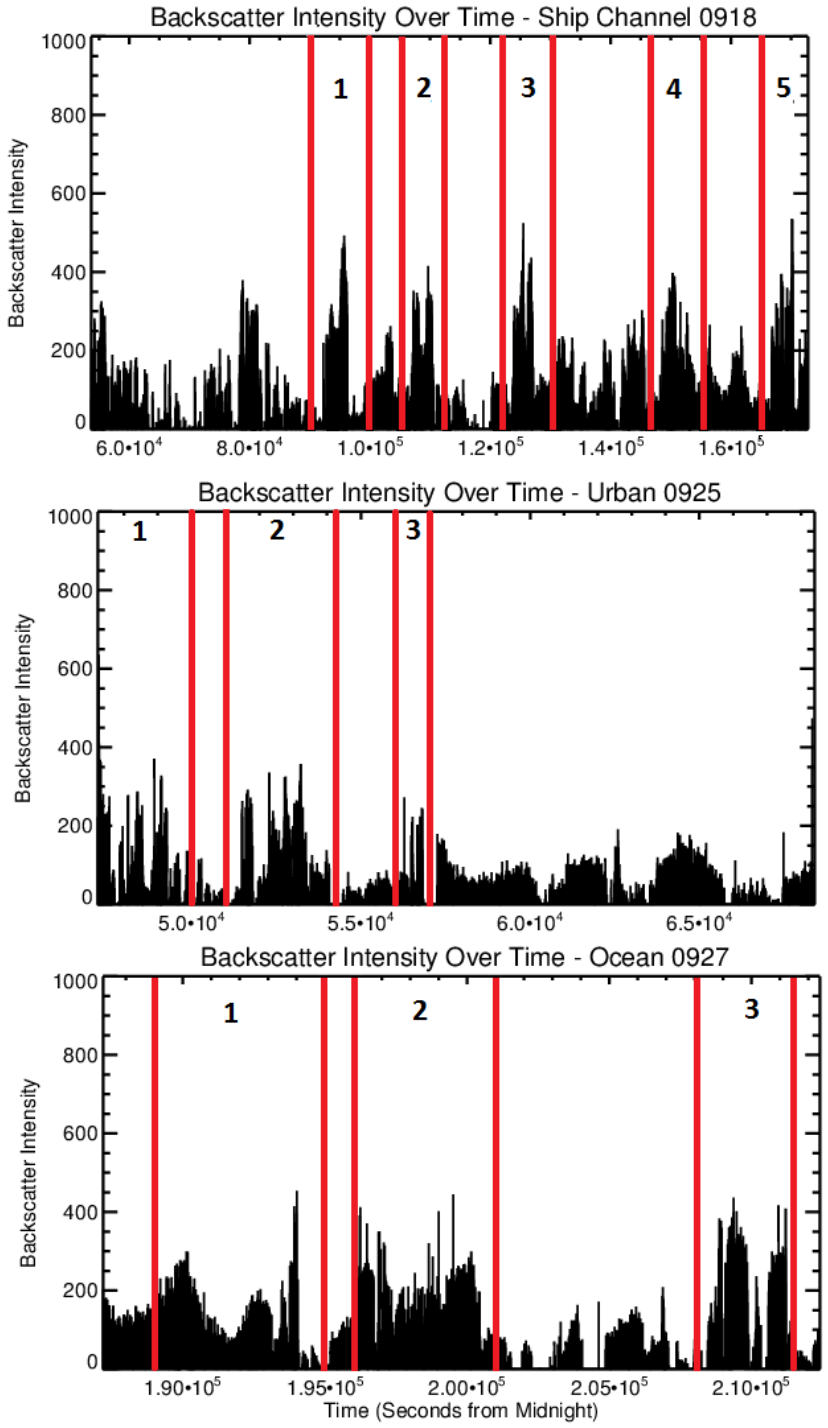

Figure 3.19: The total backscatter intensity over time, in seconds from midnight, for the Ship Channel 0918 case. The area enclosed in the red bars from 9.0 x 10^4 - 1.0 x 10^5 is the peak in total backscatter intensity that was used in the Ship Channel 0918 short case.

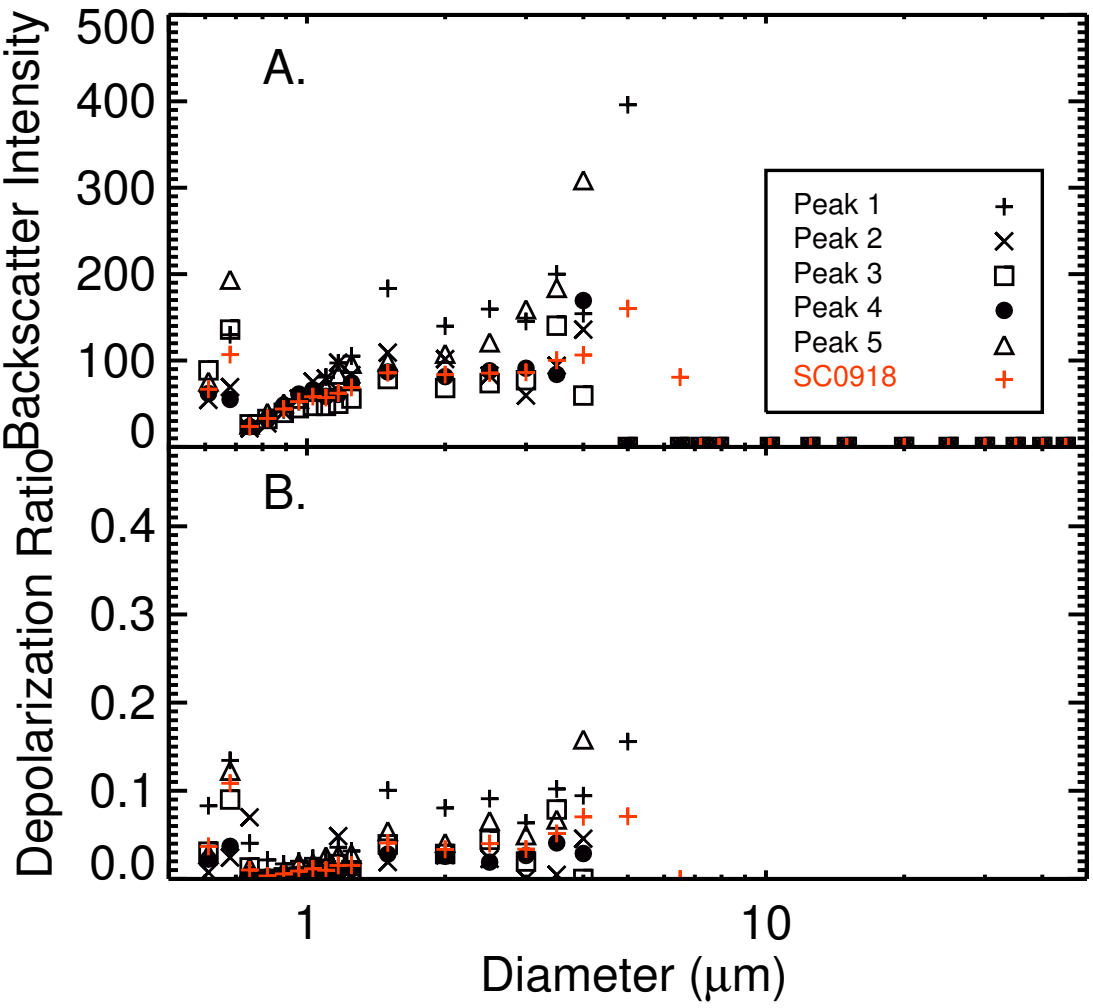

Figure 3.20: The backscatter intensity (A) and the depolarization ratio (B) as a function of particle diameter for the full Ship Channel 0918 case (red) and the five short peaks found in the backscatter intensity in the 0918 Ship Channel case.

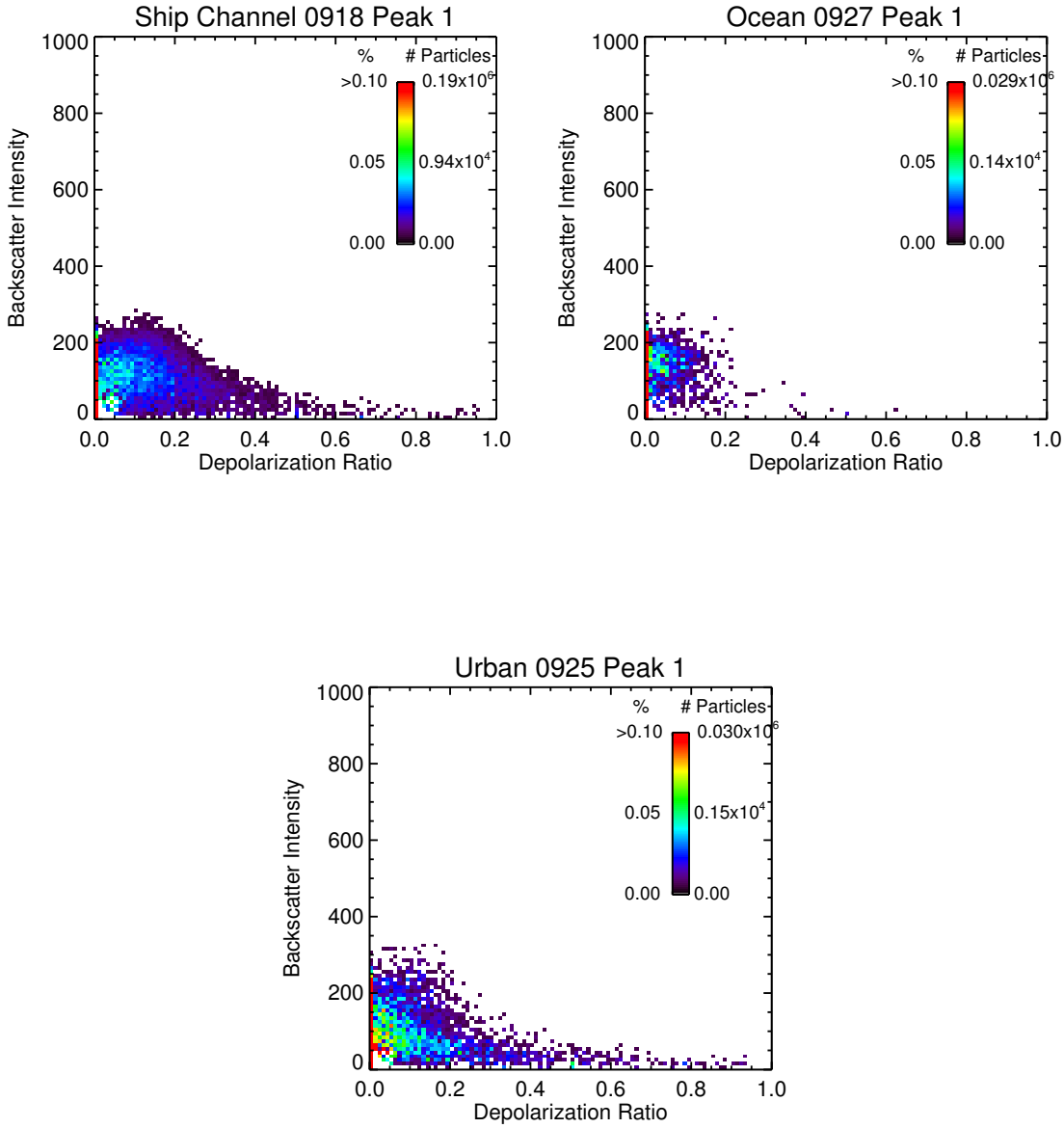

Figure 3.21: The scattering signatures for the first peak in the backscatter intensity over time plots for the Ship Channel 0918, Ocean 0927, and the Urban 0925 cases.

4. AN ANALYSIS OF HOW SOOT AFFECTS THE CLIMATE DIRECTLY AND INDIRECTLY

4.1 Optical Properties of Soot

Optical properties of freshly emitted soot were studied by generating soot in our laboratory at Texas A&M University, and using the CASPOL. A modified Santoro-type laminar diffusion burner (Santoro et al. 1983) was used to generate soot particles by the incomplete combustion of propane - compressed air mixture. The propane flow rate was approximately 0.75 mL min^{-1}, and the compressed air flow rate was $\sim$1.7 L min^{-1}. On top of the burner, a glass chimney was placed on top of the burner to protect the flame and the particle flow from being influenced by the ambient air. The flame was maintained at approximately three to four inches in height, and $\sim$3.5 inches above the top of the flame was the aerosol inlet. The flow into the inlet was 1.2 L min^{-1}, the standard flow rate of the CASPOL. A schematic of the experimental soot generation and optical properties measurement setup is shown in Figure 4.1.

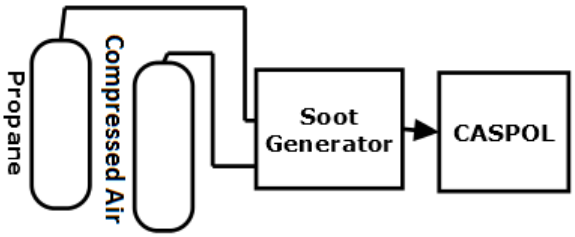

Figure 4.1: A schematic of the experimental setup used to generate fresh soot particles and measuring their optical properties using the CASPOL

The optical properties of freshly emitted soot that were generated in our laboratory are seen in Figure 4.2. As seen in Figure 4.2A, the backscatter intensity as a function of particle size, greatly increases for sizes from 0.6 – 1.0 μm. After 1.0 μm, the backscatter intensity decreases greatly. There is an exception to this however. The first soot sample (Soot 1), sampled on 06/23, has a fairly consistent backscatter intensity at all sizes which is generally less than the other soot samples. In Figure 4.2B, the depolarization ratio as a function of particle diameter is shown. The first soot sample (Soot 1) and the fourth soot sample (Soot 4), sampled on 07/09, have very similar increases in depolarization ratio until approximately 1.5 μm. After 1.5 μm, the depolarization ratio decreases to almost zero for most of the larger sizes. The first soot sample (Soot 1) has very low depolarization ratio for sizes up to 2.5 μm where the depolarization ratio increases suddenly. The third soot sample (Soot 3), collected on 06/30, has very low depolarization ratios for all sizes. Three of the four samples of freshly emitted soot particles have very similar backscatter intensities. However only two out of four of the soot samples have similar depolarization ratios.

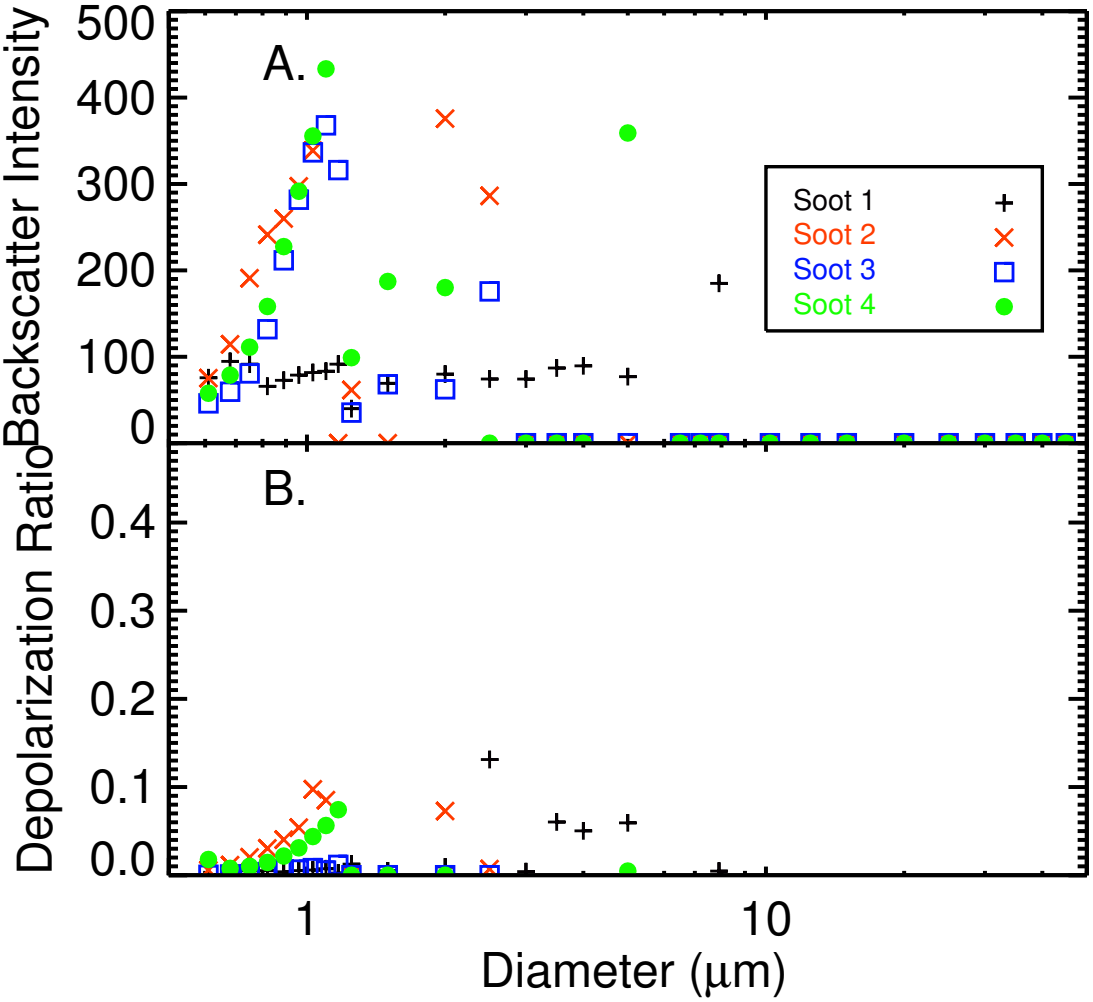

Figure 4.2: The backscatter intensity (A) and depolarization ratio (B) as a function of particle diameter for four different samples of freshly generated soot.

Scattering signatures for each of the soot samples were created (Figure 4.3). As seen in Figure 4.3, there is large variability between each soot sample. Soot samples 2 and 4 are very similar in shape with the fourth sample having a higher backscatter intensity. There are very few particles in the first soot sample. An outline similar to the shapes of the second and fourth samples is visible in the third soot sample. However, the third sample has much less particles. In all of the soot samples, there are large amounts of particles with depolarization values of zero. This indicates that there were spherical particles in the sample. It is well known that soot is not spherical at all. Thus these spherical particles must be droplets formed from condensation occurring in the line. The variation of backscatter intensity at depolarization ratio values greater than zero between the four samples could potentially be caused by soot conglomerating and forming larger soot particles with odd chain-like structures. Unfortunately, the soot samples scattering signatures are not similar to the Ship Channel, the Ocean, or the Urban scattering signatures which were previously examined in this manuscript. Thus one could reasonably conclude that soot that was sampled in-situ in Houston are mostly aged, not freshly emitted.

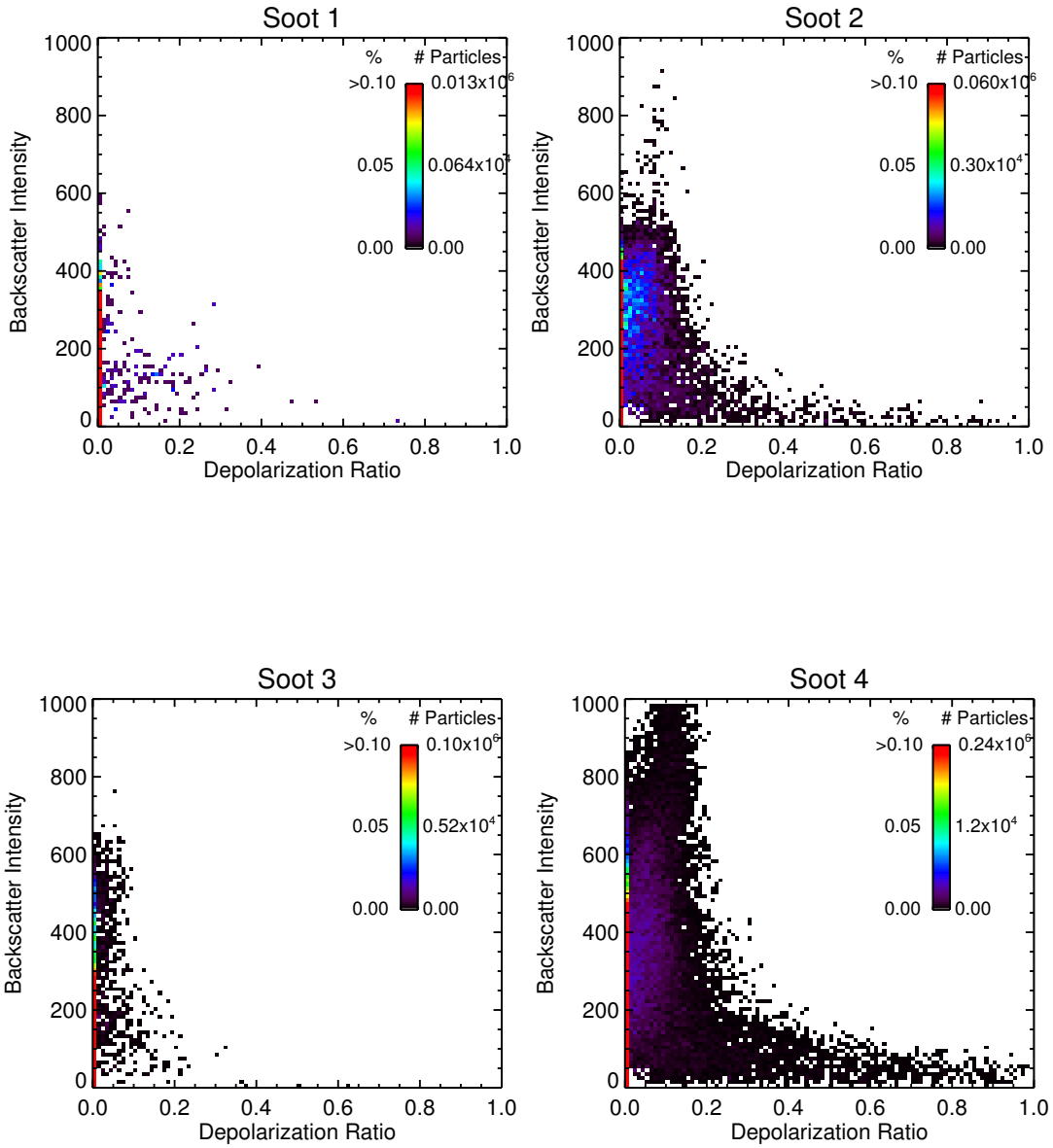

Figure 4.3: The scattering signatures for the four different samples of freshly emitted soot generated in our laboratory.

4.2 Optical Properties of Ice Nucleated onto Soot

Ice crystals are formed by two different mechanisms; homogeneous and heterogeneous nucleation (Vali 1999). Homogeneous nucleation occurs to an aqueous solution droplet at temperatures below -40 °C. While heterogeneous nucleation requires an aerosol, known as the ice nucleus (IN), to occur. Also, heterogeneous nucleation occurs at temperatures warmer than approximately -36 ° (Isono 1955; Vali 1999). Heterogeneous nucleation takes place via condensation, immersion, contact, and deposition freezing. Condensation freezing occurs when water vapor condenses on to the IN and then freezes, while immersion freezing occurs when the IN has been enveloped by liquid water for some amount of time before the freezing begins (Fukuta and Schaller 1982). For condensation and immersion freezing to occur, the air must be above water saturation. Contact freezing occurs when an IN collides with a supercooled water droplet, and deposition freezing occurs when water vapor deposits on to the IN. The water saturation must be below zero, but the air must still be saturated with respect to ice for deposition freezing to occur. A Continuous Flow Diffusion Chamber was employed in conjunction with the CASPOL to gather insight in to the optical properties of ice nucleated on to soot.

A Continuous Flow Diffusion Chamber (CFDC) was developed and constructed in our laboratory at Texas A&M University (Glen 2013) and has been used in both the laboratory (Glen and Brooks, 2014) and in the field (McFarquhar et al. 2011). The Texas A&M University CFDC is similar in design and operation as the Colorado State University CFDC (Rogers 1988, 1994). The CFDC consists of two concentric copper tubes. Each tube is cooled to a different temperature, usually between -10 °C and -50 °C. De-ionized water is pumped into the cooled chamber and allowed to freeze to the walls. The aerosol sample flows into the chamber from the top

surrounded by a sheath of filtered air such that the aerosol laden flow is directly in the center of the saturation gradient. A diagram of the CFDC showing the aerosol inlet, the recirculating sheath flow, the sliding plate that is used to evacuate and ice the chamber, and the separate CASPOL plate that is used to connect the CASPOL to the chamber is shown is Figure 4.4. Since the temperatures of each wall can be controlled, the supersaturation can also be controlled. Thus the CFDC can be used to measure the potential of an aerosol to act as an ice nucleus (IN). It can also be used as an ice crystal generator, as it was in this study. All modes of freezing are possible in the CFDC, except for contact freezing, as the flow is laminar which will not allow for any collisions between particles and supercooled droplets. The CASPOL was attached to the bottom of the CFDC by a specially designed plate to measure the optical properties of ice nucleated onto freshly emitted soot particles.

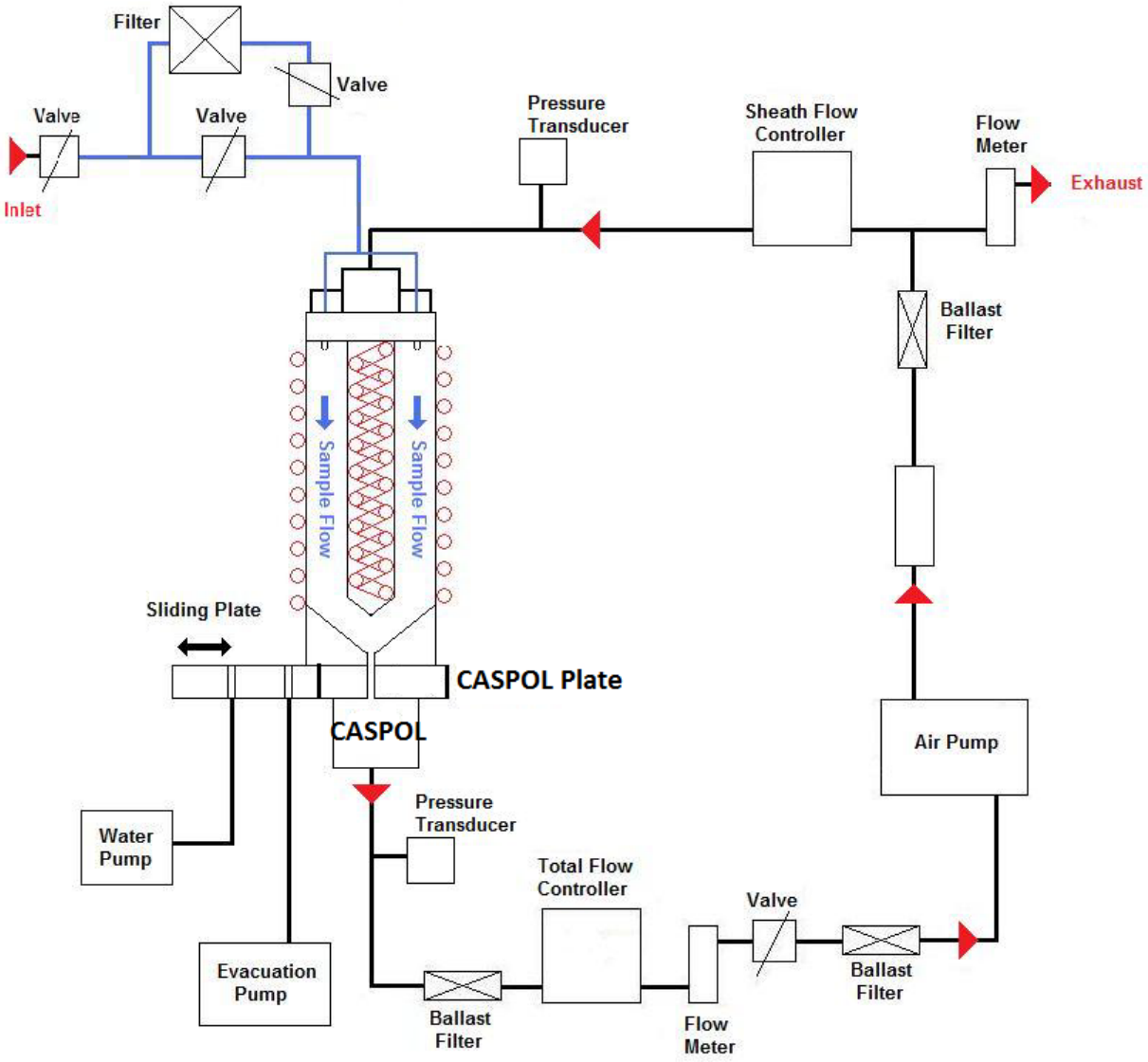

Figure 4.4: A schematic of the Continuous Flow Diffusion Chamber (CFDC) showing the aerosol inlet and the recirculating sheath flow. To evacuate and ice the chamber, a sliding plate is used to connect a water and air pump. A separate CASPOL plate is used to connect the CASPOL to the CFDC for optical property measurements. (Adapted from Glen 2013).

The Texas A&M CFDC was used in conjunction with the CASPOL to measure the optical properties of ice that has been nucleated on soot. Soot was generated in a modified Santoro-type soot generator (Santoro et al. 1983), by the incomplete combustion of propane. The soot flow passes through a desiccant dryer and to a BGI 0.732 Sharp Cut Cyclone Impactor which removed particles larger than 1.5 μm. Next, the particle flow went through a TSI 3080 Electrostatic Classifier to size select the flow to 50, 100, or 200 nm in diameter. After, the poly-disperse flow entered a mixing chamber and then flow went through a pre-cooler which was chilled to -13 °C using a Polyscience Cooling Bath. Finally the flow enters the top of the CFDC where the aerosol location temperature was held around -40 °C using two Thermo ULT 80 cooling baths. The supersaturation with respect to ice (SSI) was held between 100 and 275%, and the supersaturation with respect to water was between 30 and 130%. Thus it is safe to assume that all freezing was heterogeneous and occurred via deposition and condensation freezing modes. A schematic of the experimental laboratory setup is shown in Figure 4.5.

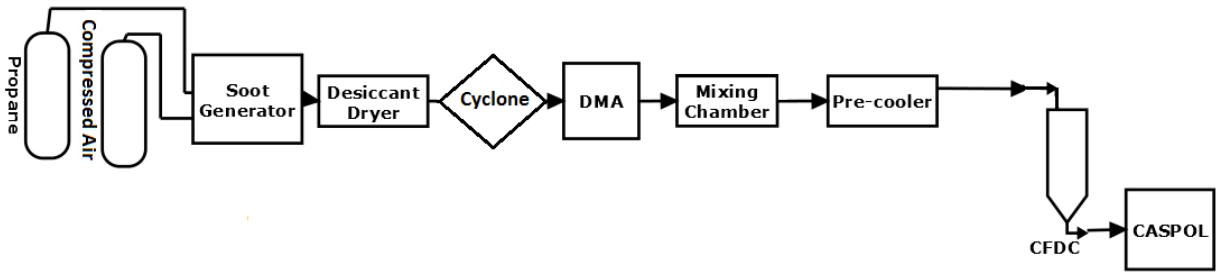

Figure 4.5: A schematic of the experimental setup of the study of the optical properties of ice nucleated on soot particles using the Texas A&M University CFDC to generate the ice crystals and the CASPOL to measure the optical properties of the crystals.

Optical properties of heterogeneous ice nucleated on two samples of freshly gen-

erated soot particles are seen in Figure 4.6. For the first sample of ice on soot, the electrostatic classifier was bypassed, so soot particle sizes were approximately 1.5 μm. For the second ice on soot sample, the soot passed through the cyclone impactor and the electrostatic classifier, with soot sizes at 50, 100, and 200 nm. In Figure 4.6, the average backscatter intensity and depolarization ratio are plotted as a function of particle diameter for ice that was nucleated onto soot particles and freshly generated soot. To eliminate any possibility of soot particles that did not have ice nucleate on them, it was decided that only particles above 1.5 μm in diameter are ice crystals, indicated by the red vertical line at approximately 1.5 μm. As can be seen, the backscatter intensity is relatively constant between 1.5 and 8 μm, as is the depolarization ratio. At diameters above 8 μm, the backscatter intensity increases exponentially, while the depolarization ratio generally decreases. In the three size bins above 1.5 μm where freshly generated soot was detected, are similar in backscatter intensity to the ice nucleated on soot, but not similar at all to the depolarization ratio. The two samples of ice crystals nucleated on to soot particles are very similar in backscatter intensity and depolarization ratio. The decrease in depolarization ratio for particles greater than 9 μm in diameter is intriguing. The size distribution for both ice on soot samples is shown in Figure 4.7. In the first ice on soot sample, there are few particles ($\sim$10 or less) larger than 10 μm. However, in the second ice on soot sample, there are many (greater than 50) particles up until the 30 μm size bin. Thus the drop in depolarization ratio at particles with diameter greater than 9 μm is not necessarily due to a lack of particles. It might potentially be caused by the shape the ice forms on the soot particles.

Optical properties of ice on soot were compared to the optical properties of heterogeneous ice nucleated on to four atmospherically relevant mineral dusts; Arizona Test Dust (ATD), Hematite, White Quartz, and Zeolite (Glen and Brooks, 2014).

The experimental setup is similar to the soot as ice nuclei experimental setup, except a Topas Solid Aerosol Generator (SAG) 410 was used to create a poly-disperse distribution of the four dusts, and the dusts were classified by an electrostatic classifier to 200 nm as seen in the bottom of Figure 4.8. The average backscatter intensity and depolarization ratio as a function of particle diameter for ice crystals nucleated onto soot particles and onto four mineral dusts are seen in Figure 4.9. At all particle diameters, the ice crystals nucleated onto soot particles have a higher backscatter intensity than any of the ice crystals nucleated onto mineral dusts. All four mineral dusts have low backscatter intensities until diameters above 10 μm where it. The ice crystals nucleated onto soot are more depolarizing at particle diameters where all particles are assumed to be ice crystals (¿ 1.5 μm). Also, there are ice crystals at all diameters for the ice nucleated onto soot, and only out to around 10 μm for two of the mineral dusts, ATD and white quartz. Using the CFDC, ice was able to be nucleated onto freshly emitted soot particles. The CASPOL was able to distinguish ice crystals that were nucleated onto dusts and ice crystals that were nucleated onto soot particles by observing the crystals optical properties.

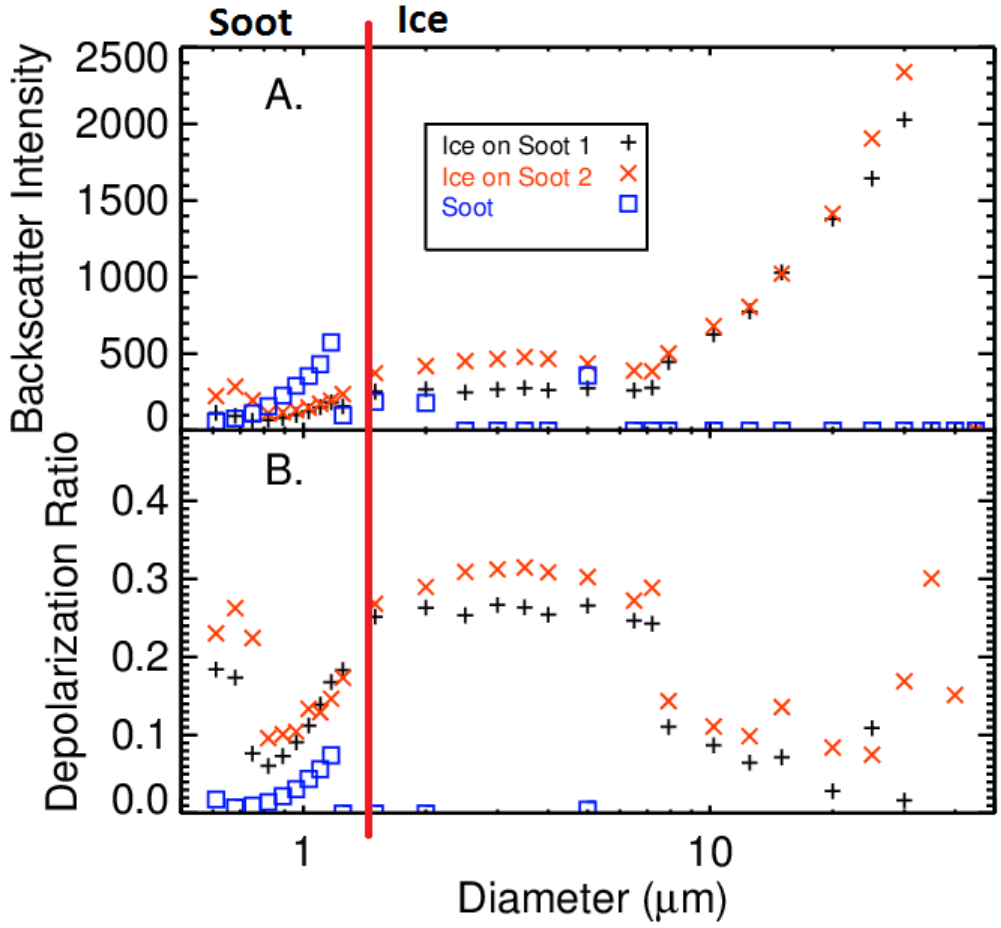

Figure 4.6: The average backscatter intensity (A) and the depolarization ratio (B) as a function of particle diameter for two samples of heterogeneous ice crystals nucleated on to soot particles and freshly generated soot. The red bar indicates the size where any particles larger than it are assumed to be entirely ice crystals.

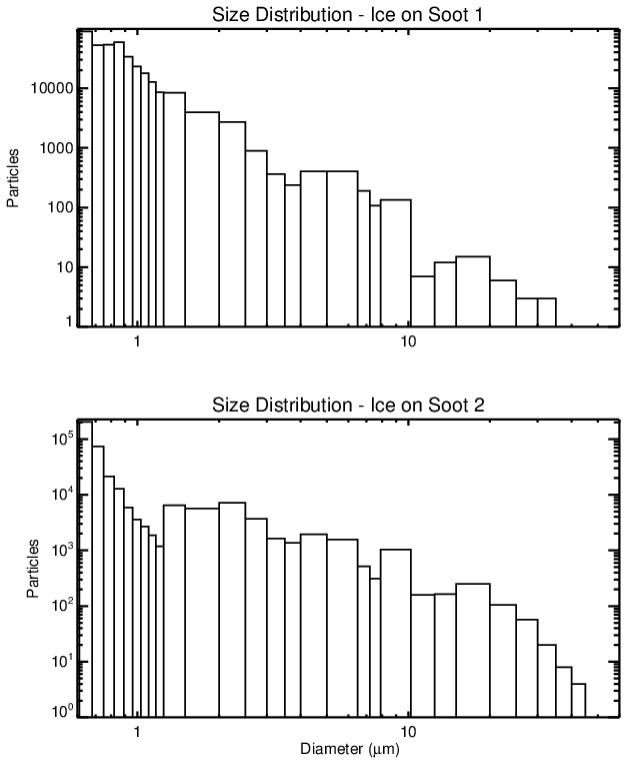

Figure 4.7: Size distributions of the first and second samples of heterogeneous ice crystals with soot as the nucleus.

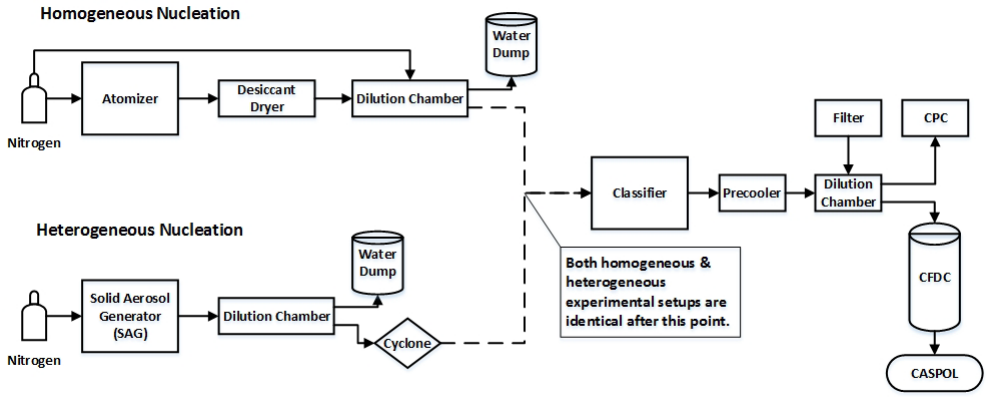

Figure 4.8: The experimental setup for the generation of homogeneous ice (Top), and heterogeneously nucleated ice with mineral dusts as nuclei (Bottom). Adapted from Glen and Brooks (2014).

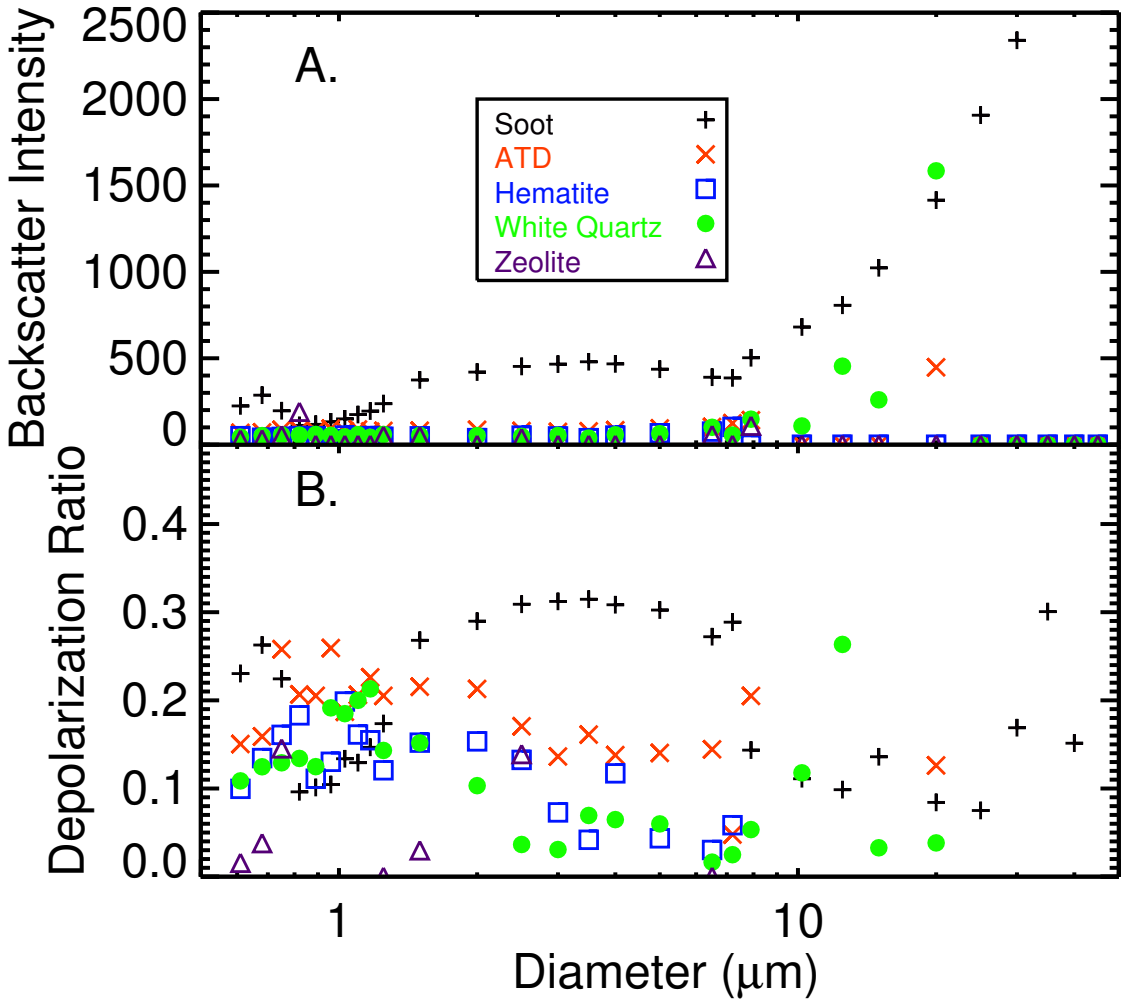

Figure 4.9: The average backscatter intensity (A) and the depolarization ratio (B) as a function of particle diameter for heterogeneous ice crystals that were nucleated onto freshly generated soot particles vs heterogeneous ice crystals that were generated onto Arizona Test Dust (ATD), Hematite, White Quartz, and Zeolite mineral dusts.

Optical properties of heterogeneous ice nucleated on to freshly generated soot particles were also compared to the optical properties of homogeneously nucleated ice. The homogeneous nucleated ice optical properties were measured by Glen and Brooks (2014). Homogeneous ice was created by atomizing a solution of ammonium sulfate (TSI 3076 Aerosol Generator). The flow of ammonium sulfate particles then flow through a desiccant dryer to remove any excess moisture and enter a large mixing chamber to dilute the concentration. Next, the flow enters the electrostatic classifier and then the pre-cooler, another mixing chamber, and then the CFDC, as seen in the top of Figure 4.8.

The average backscatter intensity and the average depolarization ratio as a function of particle diameter is shown for heterogeneously nucleated ice with freshly generated soot as the nuclei and homogeneously nucleated ice (Figure 4.10). As seen in Figure 4.10, the heterogeneously nucleated ice has a much higher backscatter intensity at nearly all diameters, although we are only considering particles with diameters greater 1.5 μm as ice crystals for ice crystals with soot as the nucleus. The bars represent plus/minus one standard deviation. According to the results from Glen and Brooks (2014), homogeneous and heterogeneously nucleated ice can not be distinguished from each other. The heterogeneously nucleated ice used in their study used four atmospherically relevant mineral dusts as the nucleus. However, with soot as the ice nucleus, heterogeneously nucleated ice can be distinguished from homogeneously nucleated ice by examining their backscatter intensities. The depolarization ratios of the heterogeneous and homogeneous ice can not be used in distinguishing the two, because the bars, which represent plus/minus one slandered deviation are completely overlapping.

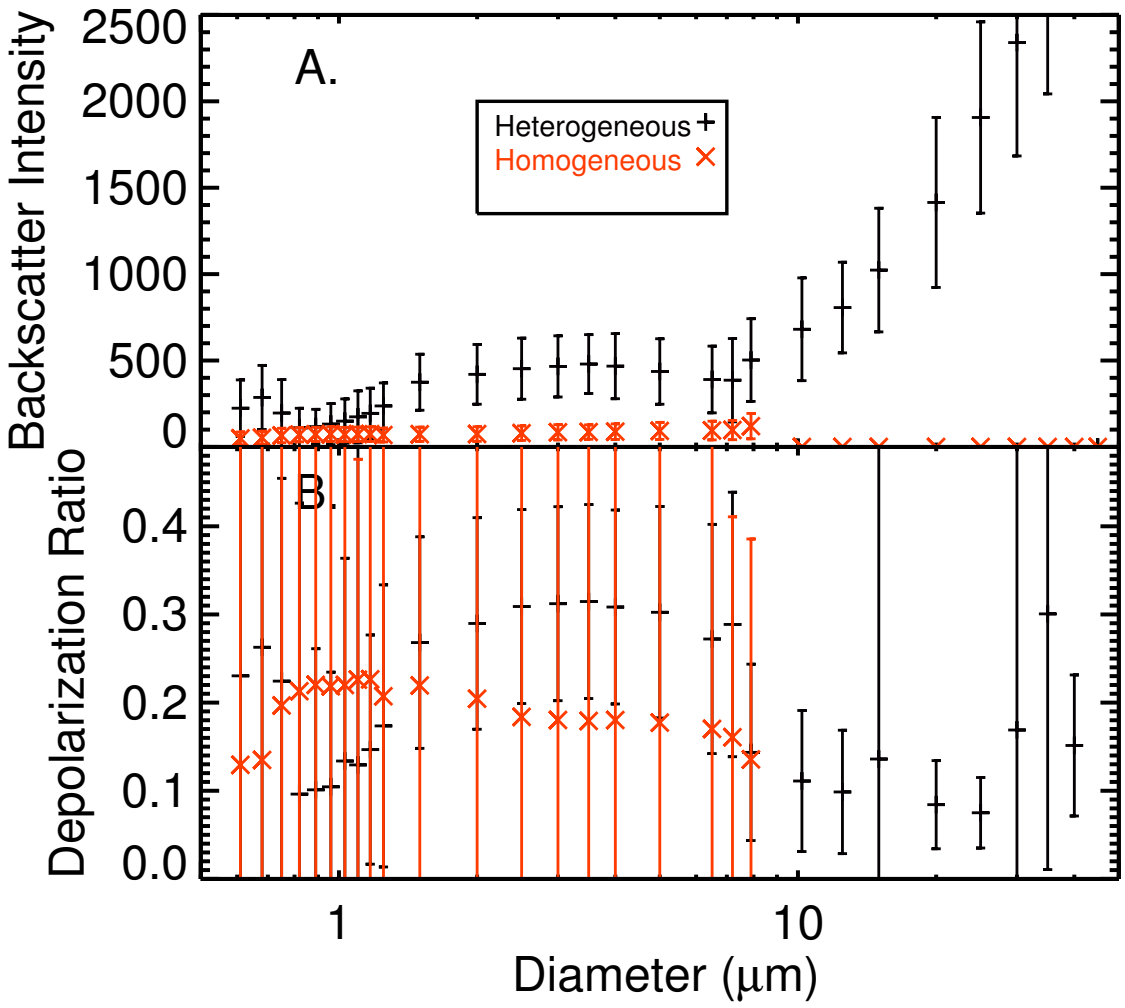

Figure 4.10: The average backscatter intensity (A) and the average depolarization ratio (B) as a function of particle diameter for heterogeneously nucleated ice using soot as the IN and homogeneously nucleated ice.

The average backscatter intensity and depolarization ratio as a function of particle diameter for each set of ice nuclei (soot) diameters, and supersaturation with respect to ice (SSI) is shown in Figure 4.11. There were three ice nuclei sizes that were selected using an electrostatic classifier, 50, 100, and 200 nm. The 50 nm soot size at both SSI values of 118% and 264% have very similar backscatter intensities at all ice crystal diameters. While the 50 nm at 118% SSI is slightly less depolarization ratios. The 100 nm at a supersaturation value of 216 % and the 200 nm also have similar backscatter intensities, and similar depolarization ratios are fairly similar at all particle diameters that are being considered as ice crystals. Also, the 100 nm and 200 nm initial ice nuclei diameter cases consists of much smaller ice crystals than the 50 nm cases. This could be due to there being more potential ice nuclei at the larger diameters, thus less water vapor would be available to grow larger ice crystals. Optical properties of ice crystals appear to be dependent on the size of the ice nucleus, and not affected by the SSI that occurred in this study.

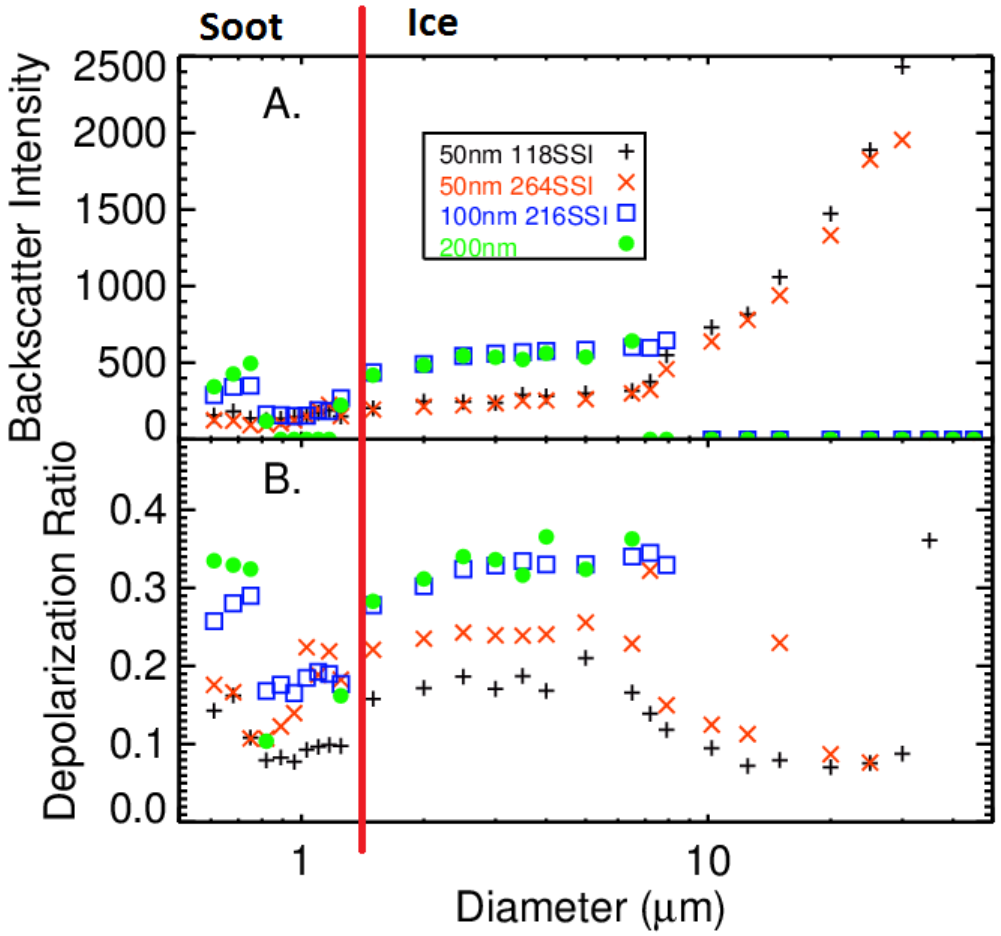

Figure 4.11: The backscatter intensity (A) and depolarization ratio (B) as a function of particle size for each initial soot particle diameter and supersaturation ratio with respect to ice.

Scattering signatures of two samples of heterogeneously nucleated ice with soot as the nucleus and heterogeneously nucleated ice with mineral dusts as the nucleus, and homogeneously nucleated ice are shown in Figure 4.12. The first ice nucleated on soot has been size selected by the cyclone impactor (Heterogeneous - Soot 1), and the second ice nucleated on soot sample is ice that was nucleated on to soot particles that were size selected by the electrostatic classifier (Heterogeneous - Soot

2). As seen, the first ice on soot example (ice on soot 1), and the second ice on soot sample (ice on soot 2) are similar in shape. However, the second ice on soot sample is more backscattering at all depolarization ratios. Both of these ice on soot samples have scattering signatures that are not similar to the scattering signatures of freshly emitted soot. The heterogeneous ice is low in backscattering intensity, less than 400 a.u., at all depolarization ratio values. The heterogeneous ice is relatively constant in the backscatter intensity at all depolarization ratios. The homogeneous ice is also very low in the backscatter intensity, less than 250 a.u. at all depolarization ratios. Unlike the heterogeneous case, the majority of the particles are low in backscattering and low in depolarization ratio. The scattering signatures can be used to distinguish ice nucleated at freshly emitted soot particles, heterogeneously nucleated ice on mineral dusts, and homogeneously nucleated ice.

The backscatter intensity distribution for the 2.5 – 3.0 μm and 7.2 – 7.9 μm is shown for freshly generated soot, the first and second samples of heterogeneously nucleated ice nucleated on soot particles, heterogeneously nucleated ice (nucleated on mineral dusts), and homogeneously nucleated ice (Figure 4.13). As seen, the backscatter intensity of soot is highly variable at both size bins, from 0 – approximately 2000 a.u. The first ice on soot sample has some variation in the backscatter intensity, but the majority of the particles have a backscatter intensity between 150 – 500 a.u. for both the 2.5 and 7.2 μm size bins. While the second sample of ice nucleated on soot has a wide range of backscatter intensities, from 0 – approximately 2000 a.u. Also, the second soot sample does not have a large number of particles at any centered around a small range of backscatter intensities, unlike the first ice on soot sample. Both the heterogeneous ice and the homogeneous have much smaller distributions in the backscatter intensity than the two ice on soot samples and the soot. Heterogeneous ice ranges from 0 – approximately 500 a.u. at both size bins, and the homogeneous

ice ranges from 0 – approximately 900 a.u. The majority of the heterogeneous ice crystals in the 2.5 μm size bin have a backscatter intensity of approximately 200 a.u., and no peak at the 7.2 μm size bin. While the homogeneous ice crystals are mostly backscattering at approximately 150 a.u. in the 2.5 μm size bin, and between 100 and 200 a.u. in the 7.5 μm size bin. Soot and ice nucleated on soot can be distinguished from each other by examining the frequency of backscatter intensity at a single size bin. Ice on soot can also be distinguished from heterogeneously nucleated ice with mineral dusts as nuclei, and homogeneously nucleated ice.

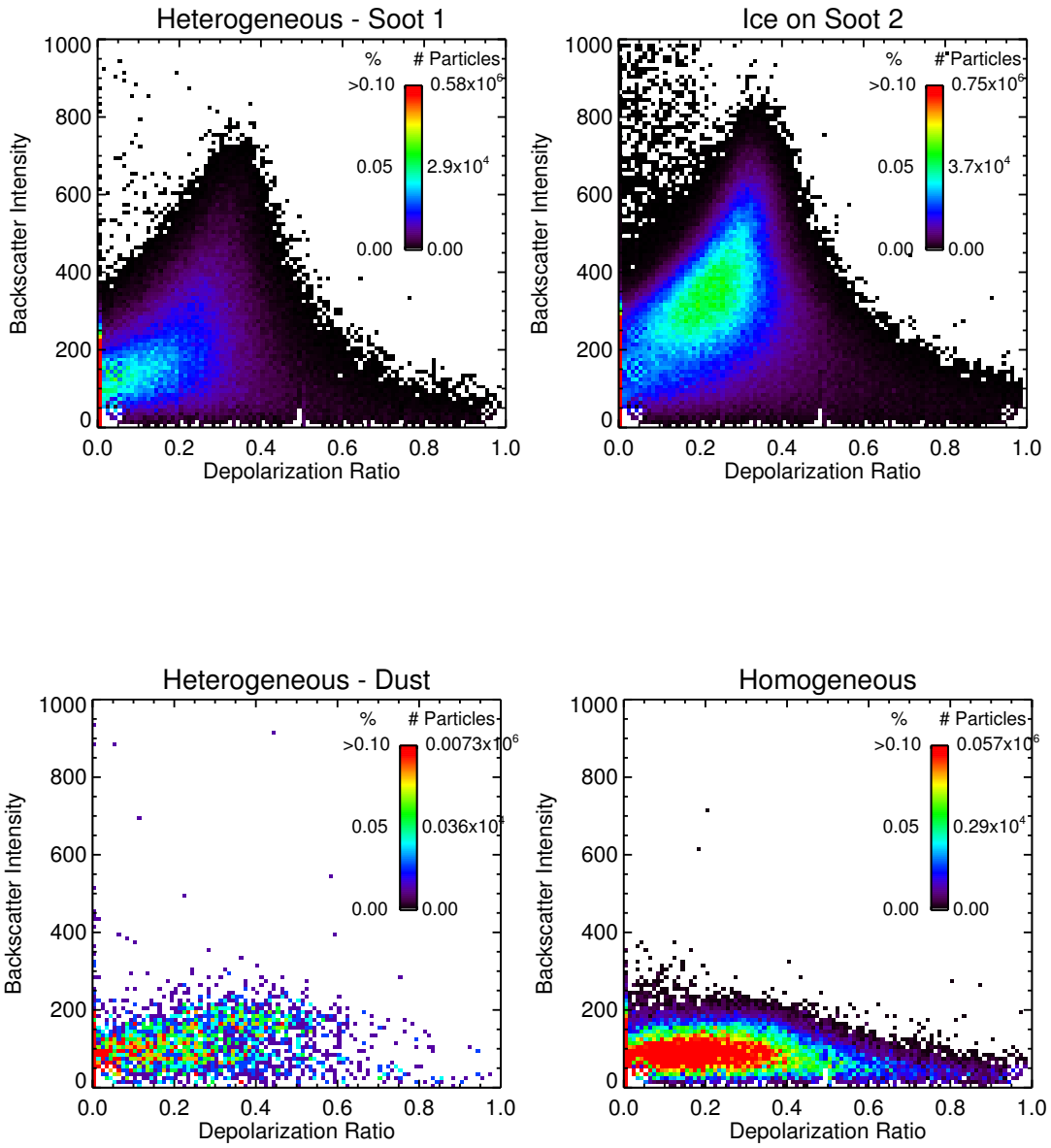

Figure 4.12: The scattering signatures for two samples of heterogeneous ice nucleated on freshly generated soot particles, heterogeneous ice nucleated on mineral dusts, and homogeneous ice.

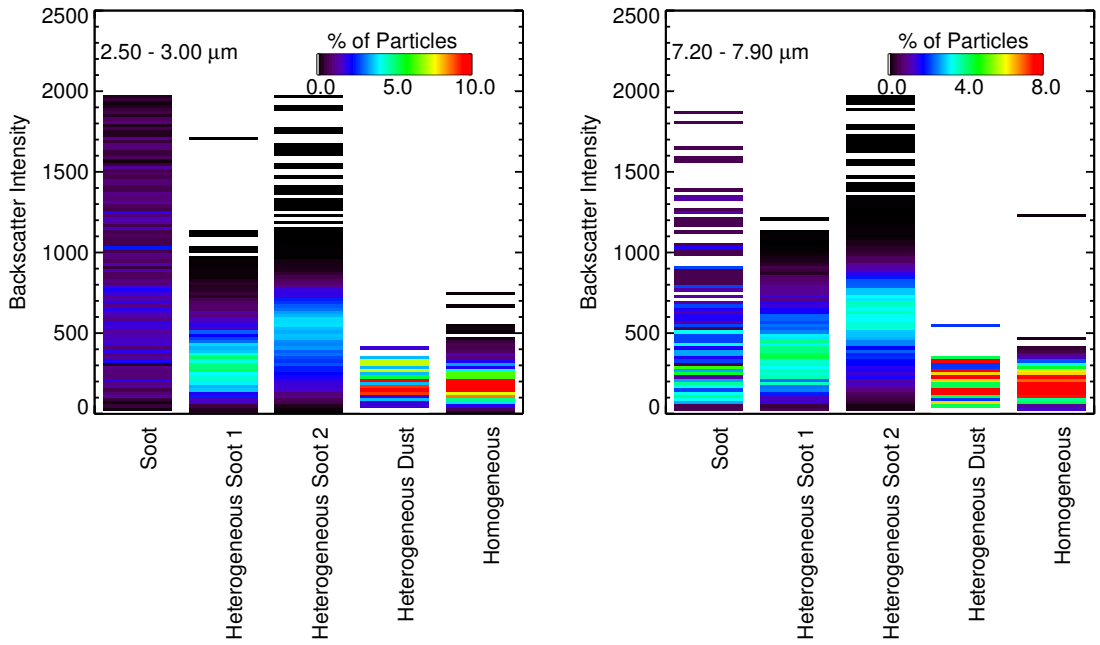

Figure 4.13: The frequency of backscatter intensity for a single CASPOL size bin for freshly generated soot, the first and second samples of heterogeneous ice nucleated on freshly generated soot particles, heterogeneously nucleated ice on mineral dusts, and homogeneously nucleated ice. Left panel is the 2.5 – 3.0 μm size bin, and the right panel is the 7.2 – 7.9 μm size bin.

5. CONCLUSIONS

The Cloud and Aerosol Spectrometer with Polarization (CASPOL), manufactured by Droplet Measurement Technologies (DMT), is a unique optical properties instrument. Two features of the CASPOL set it apart from other optical particle counters: it measures the optical properties on a particle-by-particle basis, and with the addition of a polarized backscatter detector, a depolarization ratio can be calculated. The CASPOL has successfully been used to differentiate dust and ice nucleated on to the dust (Glen and Brooks 2013; 2014). Urban areas are impacted by anthropogenic and biologic aerosols. Soot is a major component of the aerosols in an urban area consisting of up to 20% of the aerosol mass load. Being able to differentiate aerosol source locations in near real time could be immensely useful in providing current and short term air quality forecasts. Also, understanding the optical properties of soot, a major component of urban aerosols, and how soot affects the climate indirectly is important in reducing the uncertainty of the impact aerosols have on the climate. The CASPOL is the ideal instrument to improve aerosol monitoring and forecasting and further our knowledge of soot's direct and indirect affects on climate.

The CASPOL, manufactured by DMT, was used for the first time to make in-situ optical property measurements of aerosols in the field as part of NASA's *D*eriving *I*nformation on *S*urface conditions from *CO*lumn and *VER*tically resolved observations relevant to *A*ir *Q*uality (DISCOVER-AQ) in Houston, Texas. Number and volume distributions were measured by the CASPOL, and estimates of the $PM_{2.5}$ and PM_{10} mass concentrations were obtained from the volume distributions. Mass concentrations derived from the CASPOL aerosol optical property measurements were similar in trend to the mass concentrations measured around the Houston, Texas

area by the Texas Commission of Environmental Quality (TCEQ), with the exception of a second peak that was completely missed by the CASPOL's estimated mass concentration. The CASPOL most likely missed this peak because of its location on top of the Moody Tower, far away from any potential short term point sources, while the TCEQ monitoring stations are at the surface and near major roadways. There was also a potential for water to collect in some of the inlet tubing leading to the CASPOL which could result in a lower mass concentration. Also, the CASPOL estimated mass concentration was approximately two times larger than the measured mass concentrations for the first half of the study. Thus the CASPOL should not be used for regulatory monitoring of particulate matter mass concentrations.

Four potential large scale aerosol source locations that could be experienced at the Moody Tower were determined. They were the Ship Channel, Urban, Rural, and Ocean sources. Five day HYSPLIT back trajectories were used to identify cases of each aerosol source. Ten cases were found in the data when HYSPLIT back trajectories were consistent, indicating the wind direction was from one of the four sources. These cases rang from six to thirty hours in length. Of the ten cases identified, three were Urban cases, two Ocean, and five Ship Channel. No Rural cases were identified. The cases in each source were averaged together, and were not distinguishable by examining the average backscatter intensity or depolarization ratio. However, using a scattering signature technique developed by Glen and Brooks (2014), the three cases (Ship Channel, Ocean, Urban) could be distinguished from each other, except for the rural case as there were none. Thus, the CASPOL can distinguish aerosol sources. An estimation of aerosol age was made for each case using O_3 concentrations and OC/EC ratios. Some subtle differences between fresh and aged aerosols were found in both the optical signatures and the raw optical properties. Finally, average one and eight hour concentrations were calculated, and scattering

signatures were created. One hour of data was not enough to distinguish the cases; however, with eight hours of data, the cases are distinguishable. Backscatter over time was plotted, and peaks were examined. These peaks were approximately one half to three hours in length. It was found that if the number concentration is above 200 L^{-1}, than the CASPOL can differentiate aerosol source with only a few hours worth of data.

The CASPOL has successfully been used to determine aerosol source even with a few hours of data. It can differentiate between aerosol sources by using the scattering signature technique developed by Glen and Brooks (2013). The information gathered by the CASPOL could be used to provide deterministic actions to the public to take actions to protect health, such as staying indoors if the CASPOL shows that particulate matter is from a certain source area. These results show that the CASPOL can be used to type aerosols in near real time and that it can have an important impact as an air quality monitoring and forecasting tool.

Soot is a major component of aerosols in urban areas, and has large direct and indirect affects on the earth's climate. Because of this, the optical properties of freshly emitted soot and ice nucleated on to freshly emitted soot were studied. Fresh soot was generated in out laboratory and sampled by the CASPOL. The optical properties of the fresh soot were highly variable. At diameters up to 1 μm, three of the soot samples had very similar backscatter intensities, and two soot samples had similar depolarization ratios. However, at larger sizes both the backscatter intensity and depolarization ratio are quite varied. The scattering signatures of fresh soot are also rather varied. Three of the samples scatter signatures have the same general shape, but with different maximum backscatter intensities and depolarization ratios. The variability might potentially be caused to condensation forming in the inlet line between the soot generator and the CASPOL. No real similarities existed between

the soot scattering signatures or optical properties and the Houston cases. It can be safely assumed that particles that were sampled in Houston by the CASPOL consisted of many other types of aerosols as well as soot.

The CASPOL was connected to the Texas A&M University Continuous Flow Diffusion Chamber (CFDC) to measure the optical properties of ice crystals nucleated on freshly generated soot particles. We were successful in nucleating ice crystals on fresh soot particles. Soot particles that were sized by the electrostatic classifier and particles that were sized by the cyclone impactor had almost identical optical properties. Soot and ice nucleated on to soot particles have very different optical properties. The CASPOL can distinguish ice crystals that were nucleated on various mineral dusts and ice crystals that were nucleated on soot particles by the backscatter intensity alone. The optical properties of the ice crystals did not appear to be dependent on supersaturations with respect to ice that were examined in this study. However, the size of the ice crystal that nucleated on the soot particle did appear to be dependent on the size of the ice nucleus. Soot particles that were 50 nm produced the largest ice crystals up to 45 μm, while soot particles that were 100 and 200 nm produced much smaller ice crystals, 10 μm and smaller. This could be caused by more competition for water vapor in the CFDC due to an increase in the number of particles at the larger sizes. Scattering signatures were unique for heterogeneous ice with soot as the nucleus, heterogeneous ice with mineral dusts as the nucleus and homogeneous ice. In disagreement with results from Glen and Brooks (2014), heterogeneously nucleated ice with soot as the nucleus can be differentiated from homogeneously nucleated ice. These results imply that remote sensing products could be used to distinguish between soot from a volcanic eruption in the lower levels, and the same soot at higher levels that has nucleated ice on to it, as well as distinguishing ice crystals with soot as the nucleus from ice crystals with mineral dusts as the nucleus.

Also, remote sensing products can potentially differentiate between heterogeneously nucleated ice and homogeneously nucleated ice, which were once thought to have similar optical properties. The CASPOL has exciting potential as an air quality monitoring and forecasting tool, and as an instrument to improve our remote sensing abilities.

REFERENCES

Adachi, K. and P. R. Buseck, 2013: Changes of ns-soot mixing states and shapes in an urban area during CalNex. *Journal of Geophysical Research: Atmospheres*, **118 (9)**, 3723–3730.

Arakawa, E. T., P. S. Tuminello, B. N. Khare, M. E. Millham, S. Authier, and J. Pierce, 1998: Measurement of optical properties of small particles. Scientific Conference on Obscuration and Aerosol Research at Oak Ridge National Laboratory, 30.

Attwood, A. R. and M. E. Greenslade, 2011: Optical properties and associated hygroscopicity of clay aerosols. *Aerosol Science and Technology*, **45 (11)**, 1350–1359.

Barrero, M., J. Grimalt, and L. Cantón, 2006: Prediction of daily ozone concentration maxima in the urban atmosphere. *Chemometrics and Intelligent Laboratory Systems*, **80 (1)**, 67–76.

Baumgardner, D., J. Brenguier, A. Bucholtz, H. Coe, P. DeMott, and et al., 2011: Airborne instruments to measure atmospheric aerosol particles, clouds and radiation: A cook's tour of mature and emerging technology. *Atmospheric Research*, **102 (1)**, 10–29.

Baumgardner, D., H. Jonsson, W. Dawson, D. O'Connor, and R. Newton, 2001: The cloud, aerosol and precipitation spectrometer: a new instrument for cloud investigations. *Atmospheric Research*, **59**, 251–264.

Bi, L., P. Yang, G. W. Kattawar, and R. Kahn, 2009: Single-scattering properties of triaxial ellipsoidal particles for a size parameter range from the Rayleigh to geometric-optics regimes. *Applied Optics*, **48 (1)**, 114–26.

Bohren, C. F. and D. R. Huffman, 2008: *Absorption and scattering of light by small particles*. John Wiley and Sons.

Bond, T. C., S. J. Doherty, D. W. Fahey, P. M. Forster, T. Berntsen, and et al., 2013: Bounding the role of black carbon in the climate system: A scientific assessment. *Journal of Geophysical Research: Atmospheres*, **118 (11)**, 5380–5552.

Bond, T. C., G. Habib, and R. W. Bergstrom, 2006: Limitations in the enhancement of visible light absorption due to mixing state. *Journal of Geophysical Research*, **111 (D20)**, D20 211.

Bordignon, S., C. Gaetan, and F. Lisi, 2002: Nonlinear models for ground-level ozone forecasting. *Statistical Methods & Applications*, **11 (2)**, 227–245.

Briggs, D. J., C. de Hoogh, J. Gulliver, J. Wills, P. Elliott, S. Kingham, and K. Smallbone, 2000: A regression-based method for mapping traffic-related air pollution: application and testing in four contrasting urban environments. *The Science of the Total Environment*, **253 (1-3)**, 151–67.

Brunekreef, B. and B. Forsberg, 2005: Epidemiological evidence of effects of coarse airborne particles on health. *The European Respiratory Journal*, **26 (2)**, 309–18.

Brunelli, U., V. Piazza, L. Pignato, F. Sorbello, and S. Vitabile, 2007: Two-days ahead prediction of daily maximum concentrations of SO_2, O_3, PM_{10}, NO_2, CO in the urban area of Palermo, Italy. *Atmospheric Environment*, **41 (14)**, 2967–2995.

Caquineau, S., A. Gaudichet, L. Gomes, and M. Legrand, 2002: Mineralogy of Saharan dust transported over northwestern tropical Atlantic Ocean in relation to source regions. *Journal of Geophysical Research: Atmospheres*, **107**.

Chen, Y., S. M. Kreidenweis, L. M. Mcinnes, D. C. Rogers, and P. J. Demott, 1998: Single particle analyses of ice nucleating aerosols in the upper troposphere and lower stratosphere. *Geophysical Research Letters*, **25 (9)**, 1391–1394.

Chuang, M. T., Y. Zhang, and D. Kang, 2011: Application of WRF/Chem-MADRID

for real-time air quality forecasting over the Southeastern United States. *Atmospheric Environment*, **45 (34)**, 6241–6250.

Curtis, D. B., B. Meland, M. Aycibin, N. P. Arnold, V. H. Grassian, M. A. Young, and P. D. Kleiber, 2008: A laboratory investigation of light scattering from representative components of mineral dust aerosol at a wavelength of 550 nm. *Journal of Geophysical Research*, **113 (D8)**, D08 210.

Decesari, S., M. C. Facchini, E. Matta, M. Mircea, S. Fuzzi, A. R. Chughtai, and D. M. Smith, 2002: Water soluble organic compounds formed by oxidation of soot. *Atmospheric Environment*, **36**, 1827–1832.

DeMott, P. J., 2003: African dust aerosols as atmospheric ice nuclei. *Geophysical Research Letters*, **30 (14)**, 1732.

DeMott, P. J., Y. Chen, S. M. Kreidenweis, D. C. Rogers, and D. E. Sherman, 1999: Ice formation by black carbon particles. *Geophysical Research Letters*, **26 (16)**, 2429–2432.

Dickerson, R. R., S. Kondragunta, G. Stenchikov, K. L. Civerolo, B. G. Doddridge, and B. N. Holben, 1997: The impact of aerosols on solar ultraviolet radiation and photochemical smog. *Science*, **278 (5339)**, 827–830.

Diehl, K., S. Matthias-Maser, R. Jaenicke, and S. K. Mitra, 2002: The ice nucleating ability of pollen : Part II . Laboratory studies in immersion and contact freezing modes. *Atmospheric Research*, **61**, 125–133.

Diehl, K., C. Quick, and S. Matthias-Maser, 2001: The ice nucleating ability of pollen: Part I: Laboratory studies in deposition and condensation freezing modes. *Atmospheric ...*, **58 (2)**, 75–87.

DMT Manual, ., 2011: *The Cloud Aerosol Spectrometer with Depolarization Option Operator Manual DOC-0167 Revision C*. Boulder, Colorado, DMT.

Dominici, F., R. D. Peng, M. L. Bell, L. Pham, A. McDermott, S. L. Zeger, and J. M.

Samet, 2006: Fine particulate air pollution and hospital admission for cardiovascular and respiratory diseases. *Journal of the AMerican Medical Association*, **295 (10)**, 1127–1134.

Draxler, R. R. and G. Hess, 1997: Description of the hysplit4 modeling system. *NOAA Tech. ERL ARL-224*, 24.

Draxler, R. R. and G. Hess, 1998: An overview of the HYSPLIT4 modelling system for trajectories, disperstion and deposition. *Australian Meteorological Magazine*, **47**, 295–308.

Draxler, R. R., B. Stunder, G. Rolph, and A. Taylor, 1999: Hysplit4 users guide. *NOAA Technical Memo. ERL ARL-230*, **230**, 35.

Duce, R. and N. Tindale, 1991: Atmospheric transport of iron and its deposition in the ocean. *Limnology and Oceanography*, **36 (8)**, 1715–1726.

Fukuta, N. and R. Schaller, 1982: Ice nucleation by aerosol particles. theory of condensation-freezing nucleation. *Journal of the Atmospheric Sciences*, **39 (3)**, 648–655.

Fulton, J. D., 1966: Microorganisms of a Land Air Mass as It Traverses an Ocean Microorganisms of the Upper Atmosphere IV . Microorganisms of a Land Air Mass as it Traverses an Ocean. *Applied and Envrionmental Microbiology*, **14 (2)**, 241 – 244.

Glen, A., 2013: The development of measurement techniques to identify and characterize dusts and ice nuclei in the atmosphere. Ph.D. thesis, Texas A&M University.

Glen, A. and S. D. Brooks, 2013: A new method for measuring optical scattering properties of atmospherically relevant dusts using the Cloud and Aerosol Spectrometer with Polarization (CASPOL). *Atmospheric Chemistry and Physics*, **13 (3)**, 1345–1356.

Glen, A. and S. D. Brooks, 2014: Single particle measurements of the optical properties

of small ice crystals and heterogeneous ice nuclei. *In Review*.

Gorbunov, B., A. Baklanov, N. Kakutkina, H. Windsor, and R. Toumi, 2001: Ice nucleation on soot particles. *Journal of Aerosol Science*, **32 (2)**, 199–215.

Griffiths, P. T., J. S. Borlace, P. J. Gallimore, M. Kalberer, M. Herzog, and F. D. Pope, 2012: Hygroscopic growth and cloud activation of pollen: a laboratory and modelling study. *Atmospheric Science Letters*, **13 (4)**, 289–295.

Guldmann, J. and H. Kim, 2001: Modeling Air Quality in Urban Areas: A Cell-Based Statistical Approach. *Geographical Analysis*, **33 (2)**.

Hansen, J., M. Sato, R. Ruedy, A. Lacis, and V. Oinas, 2000: Global warming in the twenty-first century: an alternative scenario. *Proceedings of the National Academy of Sciences of the United States of America*, **97 (18)**, 9875–80.

Hiranuma, N., S. D. Brooks, J. Gramann, and B. W. Auvermann, 2011: High concentrations of coarse particles emitted from a cattle feeding operation. *Atmospheric Chemistry and Physics*, **11 (16)**, 8809–8823, doi:10.5194/acp-11-8809-2011.

Hirst, J. and G. Hurst, 1967: Long-distance spore transport. *Symposium, Society for General Microbiology*, Vol. 17, 307–344.

Huang, L. and R. Smith, 1999: Meteorologically-dependent trends in urban ozone. *Environmetrics*, **10 (1)**, 103–118.

IPCC, 2013: Climate change 2013: The physical science basis. contribution of working group i to the fifth assessment report of the intergovernmental panel on climate change. Cambridge, United Kingdom and New York, NY, USA.

Isono, K., 1955: On ice-crystal nuclei and other substances found in snow crystals. *Journal of Meteorology*, **12 (5)**, 456–462.

Jacobson, M. Z., 2001: Strong radiative heating due to the mixing state of black carbon in atmospheric aerosols. *Nature*, **409 (6821)**, 695–7.

Jacobson, M. Z., 2006: Effects of externally-through-internally-mixed soot inclu-

sions within clouds and precipitation on global climate. *The Journal of Physical Chemistry*, **110 (21)**, 6860–73.

Kalapanidas, E. and N. Avouris, 2001: Short-term air quality prediction using a case-based classifier. *Environmental Modelling & Software*, **16 (3)**, 263–272.

Kanji, Z. A. and J. P. D. Abbatt, 2010: Ice nucleation onto Arizona test dust at cirrus temperatures: effect of temperature and aerosol size on onset relative humidity. *The Journal of Physical Chemistry*, **114 (2)**, 935–41.

Khalizov, A. F., Y. Lin, C. Qiu, S. Guo, D. Collins, and R. Zhang, 2013: Role of OH-initiated oxidation of isoprene in aging of combustion soot. *Environmental Science & Technology*, **47 (5)**, 2254–63, doi:10.1021/es3045339.

Khalizov, A. F., R. Zhang, D. Zhang, H. Xue, J. Pagels, and P. H. McMurry, 2009: Formation of highly hygroscopic soot aerosols upon internal mixing with sulfuric acid vapor. *Journal of Geophysical Research*, **114 (D5)**, D05 208, doi: 10.1029/2008JD010595.

Koehler, K. A., P. J. DeMott, S. M. Kreidenweis, O. B. Popovicheva, M. D. Petters, and et al., 2009a: Cloud condensation nuclei and ice nucleation activity of hydrophobic and hydrophilic soot particles. *Physical Chemistry Chemical Physics: PCCP*, **11 (36)**, 7906–20.

Koehler, K. A., S. M. Kreidenweis, P. J. DeMott, M. D. Petters, A. J. Prenni, and C. M. Carrico, 2009b: Hygroscopicity and cloud droplet activation of mineral dust aerosol. *Geophysical Research Letters*, **36 (8)**, L08 805.

Kolehmainen, M., H. Martikainen, and J. Ruuskanen, 2001: Neural networks and periodic components used in air quality forecasting. *Atmospheric Environment*, **35 (5)**, 815–825.

Kotzick, R. and R. Niessner, 1999: The effects of aging processes on critical supersaturation ratios of ultrafine carbon aerosols. *Atmospheric Environment*, **33**,

2669–2677.

Lan, Z. J., X. F. Huang, K. Y. Yu, T. L. Sun, L. W. Zeng, and M. Hu, 2013: Light absorption of black carbon aerosol and its enhancement by mixing state in an urban atmosphere in South China. *Atmospheric Environment*, **69**, 118–123.

Lary, D., D. Shallcross, and R. Toumi, 1999: Carbonaceous aerosols and their potential role in atmospheric chemistry. *Journal of Geophysical Research*, **104 (1998)**.

Ma, Y., S. D. Brooks, G. Vidaurre, A. F. Khalizov, L. Wang, and R. Zhang, 2013: Rapid modification of cloud-nucleating ability of aerosols by biogenic emissions. *Geophysical Research Letters*, **40 (23)**, 6293–6297.

McFarquhar, G. M., S. Ghan, J. Verlinde, A. Korolev, J. W. Strapp, and et al., 2011: Indirect and semi-direct aerosol campaign: The impact of arctic aerosols on clouds. *Bulletin of the American Meteorological Society*, **92 (2)**, 183–201.

Mishchenko, M., L. Travis, R. Kahn, and R. West, 1997: Modeling phase functions for dustlike tropospheric aerosols using a shape mixture of randomly oriented polydisperse spheroids. *Journal of Geophysical Research*, **102 (14)**, 16,831–16,847.

Morgan, W. T., J. D. Allan, K. N. Bower, M. Esselborn, B. Harris, and et al., 2010: Enhancement of the aerosol direct radiative effect by semi-volatile aerosol components: airborne measurements in North-Western Europe. *Atmospheric Chemistry and Physics*, **10 (17)**, 8151–8171.

Nagendra, S. S. and M. Khare, 2006: Artificial neural network approach for modelling nitrogen dioxide dispersion from vehicular exhaust emissions. *Ecological Modelling*, **190 (1-2)**, 99–115.

Nicolet, M., O. Stetzer, F. Lüönd, O. Möhler, and U. Lohmann, 2010: Single ice crystal measurements during nucleation experiments with the depolarization detector iode. *Atmospheric Chemistry and Physics*, **10 (2)**, 313–325.

Pope, F. D., 2010: Pollen grains are efficient cloud condensation nuclei. *Environmental*

Research Letters, **5 (4)**, 6.

Pöschl, U., T. Letzel, C. Schauer, and R. Niessner, 2001: Interaction of ozone and water vapor with spark discharge soot aerosol particles coated with benzo [α] pyrene: O_3 and H_2O adsorption, benzo [α] pyrene degradation, and atmospheric implications. *The Journal of Physical Chemistry A*, **105 (16)**, 4029–4041.

Quinn, P., D. Coffman, V. Kapustin, T. Bates, and D. Covert, 1998: Aerosol optical properties in the marine boundary layer during the first aerosol characterization experiment (ace 1) and the underlying chemical and physical aerosol properties. *Journal of Geophysical Research: Atmospheres (1984–2012)*, **103 (D13)**, 16 547–16 563.

Rappazzo, K. M., J. L. Daniels, L. C. Messer, C. Poole, and D. T. Lobdell, 2014: Exposure to fine particulate matter during pregnancy and risk of preterm birth among women in new jersey, ohio, and pennsylvania, 2000–2005. *Environmental Health Perspectives*.

Rogers, D., 1994: Detecting ice nuclei with a continuous-flow diffusion chamber-some exploratory tests of instrument response. *Journal of Atmospheric and Oceanic Technology*.

Rogers, D. C., 1988: Development of a continuous flow thermal gradient diffusion chamber for ice nucleation studies. *Atmospheric Research*, **22 (2)**, 149–181.

Santoro, R., H. Semerjian, and R. Dobbins, 1983: Soot particle measurements in diffusion flames. *Combustion and Flame*, **51**, 203–218.

Sapkota, A., A. P. Chelikowsky, K. E. Nachman, A. J. Cohen, and B. Ritz, 2010: Exposure to particulate matter and adverse birth outcomes: a comprehensive review and meta-analysis. *Air Quality, Atmosphere & Health*, **5 (4)**, 369–381.

Sassen, K., 1991: The polarization lidar technique for cloud research: A review and current assessment. *Bulletin of the American Meteorological Society*, **72 (12)**, 1848

– 1866.

Savitz, D. A., J. F. Bobb, J. L. Carr, J. E. Clougherty, and et al., 2014: Ambient fine particulate matter, nitrogen dioxide, and term birth weight in new york, new york. *American Journal of Epidemiology*, **179 (4)**, 457–466.

Schurath, U. and K. H. Naumann, 1998: Heterogeneous processes involving atmospheric particulate matter. *Pure and Applied Chemistry*, **70 (7)**, 1353–1361.

Schwartz, J., 1993: Particulate air pollution and chronic respiratory disease. *Environmental research*, **62 (1)**, 7–13.

Seinfeld, J. H. and S. N. Pandis, 2006: *Atmospheric chemistry and physics: from air pollution to climate change*. John Wiley and Sons, Hoboken, New Jersey.

Smettem, K. R., 2006: *Particle Density, in Encyclopedia of Soil Science*. Taylor and Francis, London, England, 2060 pp.

Steerenberg, P. A., L. van Amelsvoort, M. Lovik, R. B. Hetland, T. Alberg, and et al., 2006: Relation between sources of particulate air pollution and biological effect parameters in samples from four european cities: an exploratory study. *Inhalation Toxicology*, **18 (5)**, 333–346.

Uematsu, M., Z. Wang, and I. Uno, 2003: Atmospheric input of mineral dust to the western North Pacific region based on direct measurements and a regional chemical transport model. *Geophysical Research Letters*, **30 (6)**, 1342.

Vali, G., 1999: Ice nucleation-theory: a tutorial. *NCAR/ASP 1999 Summer Colloquium*, 14–25.

von Blohn, N., S. K. Mitra, K. Diehl, and S. Borrmann, 2005: The ice nucleating ability of pollen. *Atmospheric Research*, **78 (3-4)**, 182–189.

Voukantsis, D., K. Karatzas, J. Kukkonen, T. Räsänen, A. Karppinen, and M. Kolehmainen, 2011: Intercomparison of air quality data using principal component analysis, and forecasting of PM_{10} and $PM_{2.5}$ concentrations using artificial

neural networks, in Thessaloniki and Helsinki. *The Science of the Total Environment*, **409 (7)**, 1266–76.

Wang, C., 2013: Impact of anthropogenic absorbing aerosols on clouds and precipitation: A review of recent progresses. *Atmospheric Research*, **122**, 237–249.

West, R., L. Doose, A. Eibl, M. Tomasko, and M. Mishchenko, 1997: Laboratory measurements of mineral dust scattering phase function and linear polarization. *Journal of Geophysical Research*, **102 (14)**, 16,871–16,881.

Wu, S., F. Deng, Y. Hao, X. Wang, C. Zheng, and et al., 2014: Fine particulate matter, temperature, and lung function in healthy adults: Findings from the hvnr study. *Chemosphere*, **108**, 168–174.

Yahya, K., Y. Zhang, and J. M. Vukovich, 2014: Real-time air quality forecasting over the southeastern United States using WRF/Chem-MADRID: Multiple-year assessment and sensitivity studies. *Atmospheric Environment*, **92**, 318–338.

Yin, Y., S. Wurzler, Z. Levin, and T. Reisin, 2002: Interactions of mineral dust particles and clouds: Effects on precipitation and cloud optical properties. *Journal of Geophysical Research*, **107 (D23)**, 4724.

Zhang, Y., 2004: Development and application of the Model of Aerosol Dynamics, Reaction, Ionization, and Dissolution (MADRID). *Journal of Geophysical Research*, **109 (D1)**.

Zhang, Y., M. Bocquet, V. Mallet, C. Seigneur, and A. Baklanov, 2012: Real-time air quality forecasting, part I: History, techniques, and current status. *Atmospheric Environment*, **60**, 632–655.

Zhang, Y., P. Liu, X. H. Liu, B. Pun, C. Seigneur, M. Z. Jacobson, and W. X. Wang, 2010a: Fine scale modeling of wintertime aerosol mass, number, and size distributions in central California. *Journal of Geophysical Research*, **115 (D15)**.

Zhang, Y., Y. Pan, K. Wang, J. D. Fast, and G. a. Grell, 2010b: WRF/Chem-

MADRID: Incorporation of an aerosol module into WRF/Chem and its initial application to the TexAQS2000 episode. *Journal of Geophysical Research*, **115 (D18)**.

Zhang, Y., K. Sartelet, S. Zhu, W. Wang, S. Y. Wu, and et al., 2013: Application of WRF/Chem-MADRID and WRF/Polyphemus in Europe – Part 2: Evaluation of chemical concentrations and sensitivity simulations. *Atmospheric Chemistry and Physics*, **13 (14)**, 6845–6875.

Zuberi, B., K. S. Johnson, G. K. Aleks, L. T. Molina, and M. J. Molina, 2005: Hydrophilic properties of aged soot. *Geophysical Research Letters*, **32 (1)**.